On the evaluation of the Bauschinger effect in an austenitic stainless steel—The role of multi-scale residual stresses

Jianan Hu[a], Bo Chen[b], David J. Smith[c*], Peter E.J. Flewitt[d], Alan C.F. Cocks[a]

[a] *Department of Engineering Science, University of Oxford, OX1 3PJ, UK*

[b] *The Institute for Advanced Manufacturing and Engineering, Coventry University, CV6 5LZ, UK*

[c] *Department of Mechanical Engineering, University of Bristol, BS8 1TR, UK*

[d] *H.H. Wills Physics Laboratory, School of Physics, University of Bristol, BS8 1TL, UK*

Abstract

In this work, a physically based self-consistent model is developed and employed to examine the microscopic lattice response of pre-strained Type 316H polycrystalline austenitic stainless steel subjected to uniaxial tensile and compressive loading. The model is also used to explain the Bauschinger effect observed at the macroscopic length-scale. Formulated in a crystal based plasticity framework, the model incorporates detailed strengthening effects associated with different microstructural elements such as forest dislocation junctions, solute atoms and precipitates on individual crystallographic slip planes of each individual grain within the polycrystal. The elastoplastic response of the bulk polycrystal is obtained by homogenizing the response of all the constituent grains using a self-consistent approach. Micro-plasticity mechanisms and how these influence the Bauschinger effect are illustrated in terms of the role of residual stresses at different length-scales. Overall, predictions are in good agreement with experimental data of the Bauschinger effect and the corresponding meso-scale lattice response of the material, with the latter measured by neutron diffraction. The results demonstrate that transient softening of the material is related to residual stresses at different length scales. In addition, the (Type III) residual stress at the micro-scale slip system level extends the strain range over which the tensile and compressive reloading curves of the pre-strained material merge.

Keywords: Bauschinger effect, Austenitic stainless steel, Self-consistent model, Multi-scale residual stress, microstructure

*In memory of Professor David Smith, who died as the result of a tragic climbing accident during the period this paper was in preparation.

Nomenclature

T	Absolute temperature, or the orientation matrix for individual grains
G	Shear modulus
b	Length of the Burgers vector
τ_d, τ_p, τ_s	Internal resistance associated with forest dislocation junctions, precipitates (Orowan strength) and solute atoms
$\alpha_d, \alpha_p, \alpha_s$	Obstacle strength of forest dislocation junctions, precipitates and solute atoms
τ_{cr}	Overall internal resistance or critical resolved shear strength (CRSS)
L_d, L_p, L_s	Mean spacing between forest dislocation junctions, precipitates and solute atoms on individual slip planes
N_d, N_p	Number density of forest dislocation junctions per unit area and of precipitates per unit volume
$\Delta N_{self}, \Delta N_{latent}$	Increment of dislocation segments on self- and latent- hardened slip planes
ΔN_l	Increment of number of secondary dislocation loops or segments
j_s, j_l	Self- and latent- hardening coefficient
f_v, f_A	Volume and area fraction of precipitates
r_p	Mean size (radius) of precipitates
τ_m^r, τ_p^r	Type III internal stress in the matrix and precipitates
$\dot{\gamma}_0$	Reference shear strain rate
β	Number of slip system
R	Rotational matrix
σ^a, ε^a	Stress-strain field in individual grains
L^a, C^a	Stiffness and compliance matrix of an anisotropic grain
L^i, C^i	Stiffness and compliance matrix of the isotropic polycrystal
$\varepsilon^{ta}, \varepsilon^{t*}$	Misfit strain (mismatch) in the real inhomogeneous inclusion and equivalent homogeneous inclusion
S^i	Eshelby shape tensor
X^a	Type II internal stress in individual grains
c	Solute concentration in the matrix

1. Introduction

The detailed way that a polycrystalline metal or alloy strain hardens, namely how the flow stress evolves with inelastic deformation, has been of continuous interest for over a century. Mechanisms vary with temperature and stress as demonstrated by the Ashby type deformation-mechanism maps **(Frost and Ashby, 1982)**. Many constitutive models have been proposed or developed in an attempt to understand the underlying mechanisms of strain hardening, such as the unified viscoplasticity model and its extensions **(Chaboche, 1986; Chaboche et al., 2013; Hu et al., 1992)**, and the unified phenomenological models proposed by Miller and co-workers **(Miller, 1976)**. These models have seen successful applications in a variety of problems, such as cyclic uniaxial and multi-axial loading of different materials **(Abdel-Karim and Ohno, 2000; Chaboche et al., 2013; Taleb et al., 2014)**. However, the main drawback associated with the development of macroscopic polycrystal models of these types is that there are many empirical extensions and a large number of fitting parameters, which may limit the ability to understand the role of different underlying physical deformation mechanisms **(Hu, 2015)**. More recently, crystal based plasticity models combined with the finite element method (CP-FEM) have been proposed and developed extensively to study plastic deformation arising from slip on different slip systems (see, e.g. **(Lee et al., 2010; Li and O'Dowd, 2011; Li et al., 2014; Neil et al., 2010)**). However, the work hardening behaviour in these approaches is generally only described empirically. The development of physically based deformation models based on an in-depth understanding of the internal processes that give rise to plastic deformation still remains a significant challenge **(Chen et al., 2015a; Pham et al., 2013)**.

A material's internal state is understood to be related to the distribution or density of different microstructural elements, such as forest dislocations, dislocation cell structure, solute atoms and precipitates, where precipitates have been identified to play multiple roles to strain hardening **(Ashby, 1966; Fribourg et al., 2011; Han et al., 2006; Hu and Cocks, 2015)**. From a more macroscopic, mechanistic perspective, the internal state has been classified into internal resistance and internal stress **(Chen et al., 2015a)**. The internal resistance has been identified as the intrinsic resistance to dislocation motion provided by different obstacles **(Pham et al., 2013)**, and is expressed in terms of the critical resolved shear strength (CRSS) of a slip system in the crystal plasticity framework **(Hu and Cocks, 2016b)**. The internal stress has been demonstrated to be equivalent to the residual stress that helps maintain internal equilibrium within a stress-free body, which is heterogeneous and kinematic (directional) **(Chen et al., 2015a; Pham et al., 2013)**. In the following context, we use "residual stress" instead of "internal stress". The residual stresses are generally

classified as Type I, II and III **(Withers and Bhadeshia, 2001a, b)**. Type I self-equilibrate over a length scale comparable to the macroscopic dimension of the component. Type II self-equilibrates over a length scale comparable to crystallographic grains. This type of meso-scale residual stress is a result of strain incompatibility between grains, created by the orientation dependent elastic and plastic anisotropy **(Clausen et al., 1998; Daymond and Bouchard, 2006; Pham et al., 2013; Withers and Bhadeshia, 2001b)**. A Type III residual stress is associated with the mismatch between the soft matrix and different microstructural elements (in particular, hard precipitates or dislocation cell walls) at the micro-scale, which decreases rapidly with distance but still satisfies the self-equilibrium condition. **(Kim et al., 2012)** describe Type III residual stresses as arising from a composite effect.

The motivation of this work is to develop a robust physically based state variable model with limited fitting parameters. A suitable candidate is the self-consistent model established in our previous work **(Hu and Cocks, 2016b)**, which takes into account forest dislocation (self- and latent) hardening and solute strengthening on individual slip planes in a rate-dependent crystal plasticity framework, the elasto-plastic anisotropy of the individual grains and the development of Type II residual stresses. The model has been shown to be broadly consistent with predictions from advanced dislocation dynamics (DD) simulations, but provides a much simpler structure for capturing the essential physics at the length-scale of individual grains and dealing with their interactions to model the polycrystalline response. In this paper, we further develop the model by incorporating multiple aspects of precipitation strengthening, in particular, the development of Type III residual stresses.

The advantage of a physical based model is that parameters and state variables in the model relate to physically measureable quantities. Any physically based crystal plasticity model must therefore be able to predict the observed macroscopic response and the development of the internal state and internal residual stresses within differently orientated grains. Techniques such as neutron diffraction have been developed in recent years that allow lattice strain and residual lattice strain to be measured directly. By conducting experiments in-situ within a neutron beamline, extensive multi-scale information can be generated for the validation of constitutive models.

A straightforward loading history in which the internal state can evolve rapidly is uniaxial cyclic loading, and a simple yet important evaluation of the predictive capability of a model is its ability to predict the Bauschinger effect (i.e. after straining a material in the forward direction, either in tension or compression, it can be deformed plastically at a lower stress level in the reversed direction experienced under these types of loading histories **(Chen et al., 2015a; Orowan, 1966; Sleeswyk et al., 1978)**. In this paper we evaluate the response of an ex-service Type 316H FCC polycrystalline austenitic stainless steel used in Advanced Gas Cooled nuclear reactors in the UK. Advanced neutron

diffraction techniques are used to measure the evolution of lattice strain (and hence residual stress state) as the material is deformed. We demonstrate that the extended Hu-Cocks model predicts both the macroscopic response during reversed loading and the evolution of Type II and Type III residual stresses. We also evaluate how changes in microstructure, such as volume fraction of precipitates, influence each of these features of the material response.

Macroscopically, the Bauschinger effect is often characterized by two distinct phenomena: transient softening (σ_{ts}, the offset during the early stage of plastic deformation) and permanent softening (σ_{ps}, the offset at large strains) **(Chen et al., 2015c; Yoshida et al., 2002)**, usually measured at different strain offsets as shown schematically in Fig. 1. Permanent softening is described practically as the difference between the compressive and tensile strengths at a strain offset of about 10% **(Wilson, 1965)**. However, whether a material exhibits permanent softening has been disputed **(Sleeswyk et al., 1978)**. In this study the emphasis is placed on understanding the role of the development of multi-scale residual stresses in interpreting the extent and details of any transient and whether permanent softening occurs for the 316H stainless steel considered here.

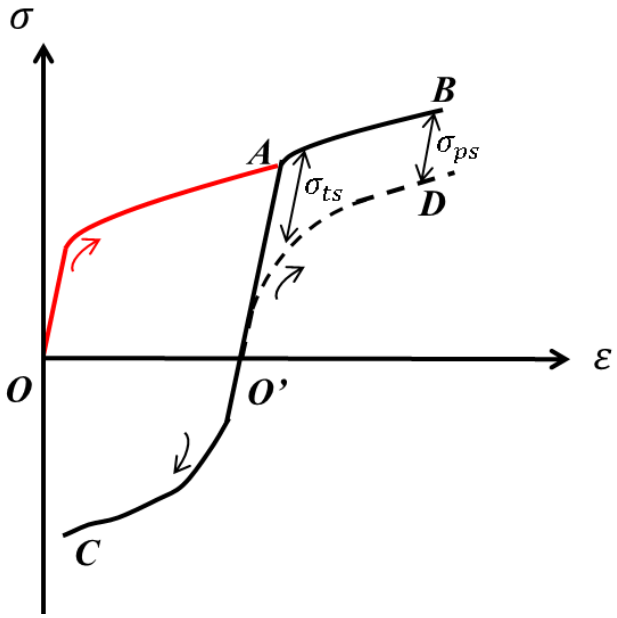

Fig. 1. Schematic diagram of Bauschinger effect, showing the prior tensile deformation history (loaded along the curve OA and unloaded along the curve AO'), together with the continued (tensile, curve O'B) and reversed (compressive, curve O'C re-plotted as O'D in absolute magnitude) straining of the material.

The layout of the paper is as follows: Section 2 describes the framework of the multi-scale self-consistent model, with precipitates and associated multiple strengthening effects incorporated (e.g. Type III residual stress). Section 3 describes a series of experiments on 316H stainless steel in which the development of elastic lattice strains during tensile/compressive loading in different grain

families are measured using neutron diffraction and related to measurements of the macroscopic Bauschinger effect. The roles of Type II and III residual stresses are examined separately in Sections 4 and 5, together with comparisons of experiments with model predictions of the macroscopic stress-strain curves and the evolution of lattice strain and residual lattice strain during both tensile and compressive reloading of tensile pre-strained specimens. Concluding remarks are given in Section 6.

2. Self-consistent model for polycrystals

The general framework of the self-consistent model developed by **(Hu and Cocks, 2016b)** consists of three sub-models, namely: dislocation link length, crystal plasticity and continuum models from micro- to the macro-scale. Here we briefly review the framework, with the main focus on the additional micromechanics elements introduced here to describe precipitation strengthening.

2.1. Dislocation link length model for individual slip planes

2.1.1. The internal resistance—critical resolved shear strength (CRSS)

Within an engineering alloy, microstructural elements such as forest dislocation junctions, solute atoms and precipitates block the motion of dislocation and divide the dislocations into segments. The internal resistance is defined as the shear stress required for a dislocation to propagate through an array of obstacles across a slip plane, which is equivalent to the classical definition of the critical resolved shear strength (CRSS). **(Foreman and Makin, 1966)** and **(Dong et al., 2010)** have formulated the CRSS for a single type of obstacle in the form $\tau=\alpha Gb/L$, where α is a dimensionless constant, L is a characteristic mean spacing between obstacles on the slip plane (see section 2.1.2), G is the shear modulus of a single crystal and b is the length of the Burgers vector. Combination of any two types of obstacle (which give rise to independent CRSSs τ_1 and τ_2) leads to a joint CRSS τ_t, given by **(Dong et al., 2010; Kocks, 1985; Picu et al., 2009)**

$$\tau_t^{\,q} = \tau_1^{\,q} + \tau_2^{\,q} \tag{1}$$

where q is an exponent between 1 and 2. **(Dong et al., 2010)** have shown that the linear superposition rule or additive strengthening (q=1) is valid when the number densities of the two obstacles differ by more than a factor of three, otherwise the geometric mean or quadratic rule (q=2) prevails. For Type 316H austenitic stainless steels employed in this work, the combined effect of forest dislocation junctions and solute atoms has been described and evaluated in our previous work

(Hu and Cocks, 2016b), where q=1. For 316H the contributions from forest and precipitation hardening are comparable to each other and an appropriate way to formulate the overall CRSS can be written as

$$\tau_{cr} = \sqrt{{\tau_d}^2 + {\tau_p}^2} + \tau_s = \sqrt{\left(\frac{\alpha_d G b}{L_d}\right)^2 + \left(\frac{\alpha_p G b}{L_p}\right)^2} + \frac{\alpha_s G b}{L_s} \tag{2}$$

Parameters with subscripts "*d, p, s*" are associated with dislocation junctions, precipitates and solid solution respectively. This form of relationship has also been used by **(Deschamps and Brechet, 1998)** and confirmed by dislocation dynamics studies **(Queyreau et al., 2009, 2010)**.

2.1.2. The state variables—mean spacing L

For forest dislocation strengthening, given a random distribution of N_d, junctions per unit area on each elementary slip plane, the mean spacing of the junctions on the slip plane, L_d in Eq.(2), can be written as $L_d = N_d^{-1/2}$. It has been shown that the random distribution of forest dislocation junctions is equivalent to the distribution of connected dislocation segments **(Hu and Cocks, 2016b)**. All the segments in a network can be considered as immobile and held-up at obstacles at any instant **(Lagneborg and Forsen, 1973)**. Free and fast glide motion of dislocations between obstacles occurs on the slip plane once the resolved shear stress (RSS) approaches the critical value τ_d. As a result, a shear strain increment $\Delta\gamma$ is generated on the slip plane until these activated segments are blocked and partitioned into shorter segments by other pre-existing or newly created junctions and become immobile again. Further glide occurs when the RSS increases and mobilizes more segments. Throughout this process, dislocations multiply and new segments or junctions are generated on each slip plane **(Alankar et al., 2012)**. Strain hardening can then be characterised by the increase of the number of dislocation segments (junctions) or the decrease of mean spacing. Note strain hardening varies on different slip planes according to the above description of the multiplication process. **(Hu and Cocks, 2016b)** have identified three sub-processes, namely (i) multiple releases, (ii) expansion, and (iii) mutual partitioning or network refinement. Self-hardening involves all three sub-processes while latent hardening only involves the last of these. Therefore, a plastic shear strain increment $\Delta\gamma$ on a single active slip plane leads to non-identical increase of the number of junctions on the self-hardened plane (ΔN_{self}) and latent hardened planes (ΔN_{latent}), which has been formulated by two independent relationships **(Hu and Cocks, 2016b)**

$$\Delta N_{self} = j_s \Delta\gamma \tag{3a}$$

$$\Delta N_{latent} = j_l \Delta\gamma \tag{3b}$$

where j_s, j_l are regarded respectively as self-hardening and latent hardening coefficients. Eqs. (3a) and (3b) update the total number of junctions N_d after an increment of plastic strain and thus give rise to the evolution of mean spacing L_d on self- and latent- slip planes. This approach in determining self- and latent hardening has been shown to be consistent with dislocation dynamics (DD) simulations **(Hu and Cocks, 2016b)** which describe self- and latent hardening by distinguishing the strength of individual junctions on different slip planes using an interaction coefficient matrix **(Devincre et al., 2006; Groh and Zbib, 2009)**. It is important to note that this model contains a number of simplifying assumptions in order to limit the number of parameters that are needed to describe the material response. The most important of these is that, as in most models of this type, we express the response associated with a given slip plane in terms of the average number of dislocation link lengths and that there is a given stress, the CRSS, at which a dislocation glides across a slip plane. In practice, a slip plane will contain a distribution of link lengths **(Lagneborg and Forsen, 1973)** and there is a gradual increase in shear strain as the stress is increased and more and more links are released. The effect of this process on the constitutive response is discussed by **Hu, (2015)**. We discuss this further in section 4 when we evaluate the experimental results.

For solid solution strengthening, the mean spacing L_s (Eq. 2) between randomly distributed solute atoms on each slip plane can be expressed as **(Hirth and Lothe, 1982; Pham et al., 2015)**

$$L_s = (cb)^{-1/2} \tag{4}$$

where c is the solute concentration or number density of all the solute atoms in the material, which can be calculated from the given chemical composition, and (cb) is the projection on a slip plane. In contrast to the approach adopted for forest dislocation strengthening, the state variable L_s has been simplified to be identical on all slip planes, i.e. variations of the distribution of solute atoms on different slip planes is ignored. L_s varies with chemical composition, which could change if the body is at a temperature where continued precipitation occurs.

In this paper we consider the additional effect of precipitation strengthening. All precipitates are idealized as spherical and non-deformable particles (**Hu, 2015**). The mean spacing between randomly distributed precipitates on a given slip plane can be expressed as a function of the volume fraction of precipitates f_v and the mean radius r_p based on Friedel's theory **(Friedel, 1964)**

$$L_p = r_p\sqrt{\frac{2\pi}{3f_v}} \qquad \text{and} \qquad f_v = \frac{4}{3}\pi {r_p}^3 N_p \tag{5}$$

where N_p is the number density of precipitates in the material. Similar to solid solution strengthening, we do not distinguish between distributions of precipitates on different slip planes, thus the state variable L_p is identical on all slip planes.

2.1.3. The role of precipitates—Orowan loops and micro-Type III internal stress

Here the emphasis is put on roles that precipitates can play in strengthening a material, depending on the nature of the dislocation-precipitate interactions. The first effect is its contribution to CRSS (Eq. 2). The dislocations bypassing precipitates via the classical Orowan bowing process (Fig. 2) and τ_p is also called Orowan strength for pairs of precipitates **(Argon, 2008; Foreman and Makin, 1966; Pham et al., 2015)**. The second effect is derived from the closed loops formed around precipitates as dislocations bypass them **(Chang et al., 2012; Hirsch and Humphreys, 1969)**. These loops, often regarded as geometrically necessary dislocations, can enhance the forest dislocation strengthening as additional links or junctions, as described in section 2.1.2. The loops shown in Fig. 2 are often called Orowan or primary loops, and the corresponding plane is called the primary plane.

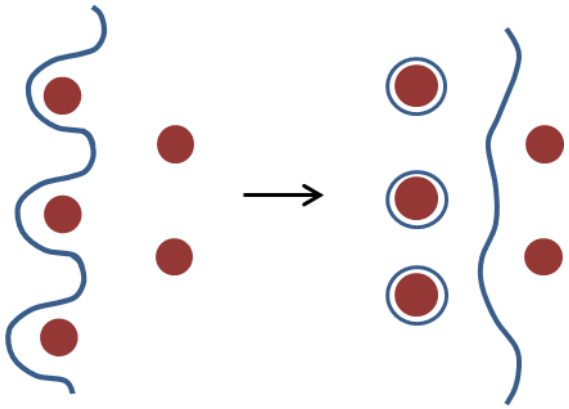

Fig. 2. The Orowan bowing bypassing mechanism, leaving loops encircling each precipitate (**Hirsch and Humphreys, 1969**)

(Ashby, 1966) and **(Brown and Stobbs, 1971)** demonstrated that the Orowan loops only occur for the first two or three dislocations that bypass a precipitate. It then becomes more energetically favourable for plastic flow to be accommodated by the punching out of prismatic loops from precipitates on secondary slip planes, with a schematic shown in Fig. 3 **(Ashby, 1966; Hirsch and Humphreys, 1969)**. Experimental support of this mechanism has been provided by **(Calhoun and**

Mortensen, 1999). These prismatic loops consist of "interstitial" loops (equivalent to those produced by condensation of interstitial atoms) and "vacancy" loops (equivalent to those produced by condensation of vacancies). A simple quantitative analysis of this and the contribution to additional forest dislocation junctions is given in **Appendix A**.

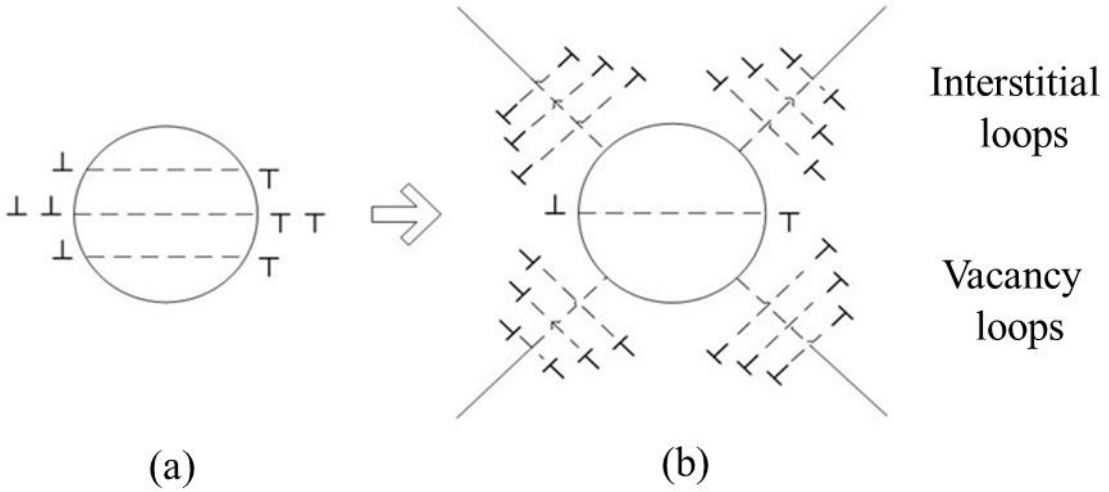

Fig. 3. A schematic illustration of the generation of primary and secondary loops. (a) Shear in the primary slip system has left primary Orowan loops around the precipitate. The primary slip plane is horizontal and perpendicular to the page. (b) Secondary slip has occurred by the nucleation and glide of secondary prismatic loops (interstitial and vacancy).

While the above two aspects of precipitate strengthening provide contributions to the internal resistance, another consequence of the development of the dislocation structures around the precipitates is that it increases the stress carried by the precipitate and therefore generates a residual state of stress in the material. We are primarily interested in the residual stress in the matrix, as it is this that determines the extent of any further dislocation motion and plastic deformation. For a slip plane containing an area fraction f_A of intersecting precipitates (identical to the volume fraction f_v for a random distribution of precipitates **(Argon, 2008)**), the stress balance on the slip plane in the stress-free state is

$$\tau_m^r(1-f_A)+\tau_p^r f_A=0 \tag{6}$$

where τ_p^r and τ_m^r are internal/residual stresses respectively in the precipitates and matrix **(Han et al., 2004)**. According to the definition described in section 1, τ_p^r and τ_m^r are Type III microscopic residual stresses. A simple analytical solution of this Type III residual stress is given in **Appendix B**, following **(Ashby, 1966)** and **(Kroupa, 1962)**, where it is shown that the residual stress state is equivalent to a pure shear stress state and is a function of f_A and the total accumulated plastic shear strain γ on the slip plane:

$$\tau_m^r \approx -0.7\alpha_d G\gamma f_A^{3/2} \tag{7}$$

However, it should be noted that different slip planes are not perpendicular to each other, thus the Type III residual stress generated by slip on a particular active slip plane will also have resolved components on other slip planes in the crystal. Thus the Type III residual stress on a given slip system is determined by the amount of slip on all slip systems in the crystal. This will be illustrated in the next section. Also, it is interesting to note that this residual stress only depends on the area (or volume) fraction of particles. It does not depend independently on the size and spacing of the particles. The residual stress depends on the number of prismatic loops punched out from the particles (that scales with the size of the particles for a given plastic strain) and the distance that the loops are punched out away from the particles (which scales with their spacing). The residual stress increases with increasing number of loops (i.e. size of particles) and decreasing distance that they are punched out (i.e. spacing of particles). These two effects combine to give a residual stress that depends on the ratio of particle size to spacing, i.e. the area fraction of particles, as illustrated in Appendix B.

2.2 Crystal plasticity framework for individual grains

The crystal plasticity framework combines the responses for each slip plane in a grain to describe the overall crystal response. The approach adopted is fully described by **(Hu and Cocks, 2016b)**. Here we provide the major relationships and new contributions that arise from the consideration of precipitate hardening. For F.C.C. materials, each individual grain contains four {111} slip planes and each slip plane has three <110> slip directions, giving a total of twelve slip systems. Following **(Asaro and Needleman, 1985), (Hutchinson, 1976),** and **(Anand and Kothari, 1996)**, a simple rate-dependent power-law relationship is employed between the plastic shear strain increment $\Delta\gamma^\beta$ and the current values of the resolved shear stress (RSS) τ^β and overall internal resistance or CRSS τ_{cr}^β on a given slip system β ($\beta = 1 \sim 12$), within a prescribed time step Δt

$$\Delta\gamma^\beta = \Delta\gamma_0 \left| \frac{\tau^\beta + \left(\bar{\tau}_m^r\right)^\beta}{\tau_{cr}^\beta} \right|^p \operatorname{sgn}\left(\tau^\beta + \left(\bar{\tau}_m^r\right)^\beta\right) \tag{8}$$

where p is a rate sensitivity exponent and $\Delta\gamma_0 = \dot{\gamma}_0 \Delta t$ is a reference shear strain increment. Coplanar systems belonging to the same slip plane are understood to have identical CRSS and experience the same hardening **(Bronkhorst et al., 1992; Hu and Cocks, 2016b; Kocks, 1970)**. Thus there are

only four independent CRSS terms τ_{cr}^{β} and $\Delta\gamma$ in Eq. (3) is simply the absolute sum of all $\Delta\gamma^{\beta}$ on the slip plane. Further, if the overall stress in a crystal is denoted as σ^{a}, and $\bar{n}^{\beta}(n_1^{\beta}, n_2^{\beta}, n_3^{\beta})$ is the normal to a slip plane and $\bar{s}^{\beta}(s_1^{\beta}, s_2^{\beta}, s_3^{\beta})$ is one of the slip directions associated with the slip system β, τ^{β} is given by

$$\tau^{\beta} = \left[sym\left(\bar{n}^{\beta} \otimes \bar{s}^{\beta}\right)\right]^{T} \sigma^{a} \tag{9}$$

where $sym\left(\bar{n}^{\beta} \otimes \bar{s}^{\beta}\right)$ is the Schmid factor of slip system β and $\otimes$ represents the dyadic product. The inclusion of precipitation hardening requires the specification of an additional term compared to the equations presented by **(Hu and Cocks, 2016b)**, i.e. the Type III residual stresses $\left(\bar{\tau}_m^r\right)^{\beta}$ on each slip system β **(Aghababaei et al., 2011; Han et al., 2004; Kim et al., 2012; Liu et al., 2011; Yu et al., 2014)**. The way of calculating $\left(\bar{\tau}_m^r\right)^{\beta}$ is as follows: firstly, micro-scale residual stress $\left(\tau_m^r\right)^{\beta}$ (Eq. 7, details in **Appendix B**) on each slip system is resolved onto the single crystal (grain) Cartesian co-ordinate system and summed to calculate a nominal residual stress term σ_m^r

$$\sigma_m^r = \sum_{\beta=1}^{12} \left(\tau_m^r\right)^{\beta} sym(\bar{n}^{\beta} \otimes \bar{s}^{\beta}) \tag{10}$$

Then, $\left(\bar{\tau}_m^r\right)^{\beta}$ can be calculated in a way similar to Eq. (9) (resolving back onto individual slip systems) **(Aghababaei et al., 2011)**

$$\left(\bar{\tau}_m^r\right)^{\beta} = \left[sym\left(\bar{n}^{\beta} \otimes \bar{s}^{\beta}\right)\right]^{T} \cdot \sum_{\beta=1}^{12} \left(\tau_m^r\right)^{\beta} sym\left(\bar{n}^{\beta} \otimes \bar{s}^{\beta}\right) \tag{11}$$

Finally, by adding all the shear strain increments $\Delta\gamma^{\beta}$ calculated from Eq. (8) on all slip systems within each individual grain, the total nominal plastic strain increment for the grain $\Delta\varepsilon^{p}$ can be obtained **(Asaro and Needleman, 1985; Kocks and Mecking, 2003)**:

$$\Delta\varepsilon^{p} = \sum_{\beta}^{12} \Delta\gamma^{\beta} sym(\bar{n}^{\beta} \otimes \bar{s}^{\beta}) \tag{12}$$

2.3. Self-consistent scheme for polycrystal aggregate

Response of a macroscopically isotropic polycrystalline aggregate, (with random distribution of grain orientations) can be characterized by a self-consistent scheme or a homogenization method

equivalent to that originally proposed by **(Budiansky and Wu, 1962; Kroner, 1961).** Full details of the approach adopted here are given by **(Hu and Cocks, 2016b).** Each individual anisotropic grain/crystal is assumed to be spherical. Given a macroscopic stress σ, the response of each inhomogeneous grain can be given by

$$\varepsilon^{ta}+\left[\left(C^a\right)^{-1}-\left(C^i\right)^{-1}\right]R\sigma=\left[\left(C^a\right)^{-1}C^i\left(I-S^i\right)+S^i\right]\varepsilon^{t*} \tag{13}$$

where C^i, C^a are respectively the elastic stiffness matrices for the isotropic bulk polycrystal and the individual anisotropic grain; S^i is a shape tensor only dependent on the geometry of the grain and Poisson's ratio of the isotropic polycrystal **(Eshelby, 1957; Mura, 1982)**. The detailed form of these and subsequent matrices can be found in **(Hu and Cocks, 2016b)**. ε^{ta} and ε^{t*} are respectively the plastic misfit strain in a grain and the equivalent homogeneous inclusion, where ε^{t*} is an important intermediate term that can be used to determine the stress in inhomogeneous/homogeneous inclusions **(Mura, 1982)**. *I* is the unity matrix and *R* is the orientation matrix of the grain in terms of the outward normal to the faces of the unit cell with respect to a local co-ordinate system **(Hu, 2015; Hu and Cocks, 2016b)**. Eq. (13) is applicable to both macroscopic elastic ($\varepsilon^{ta}=0$) and plastic ($\varepsilon^{ta}\neq 0$) deformation. During elastic deformation

$$\sigma^a=\left\{\left\{\left[I-\left(S^i\right)^{-1}\right]^{-1}\left(C^i\right)^{-1}-\left(C^a\right)^{-1}\right\}^{-1}\left[\left(C^a\right)^{-1}-\left(C^i\right)^{-1}\right]+I\right\}R\sigma=H^aR\sigma \tag{14a}$$

$$\varepsilon^a=\left\{\left(C^i\right)^{-1}+\left\{\left[\left(C^a\right)^{-1}-\left(C^i\right)^{-1}\right]^{-1}\left(C^a\right)^{-1}C^i\left(S^i\right)^{-1}-C^i\right\}^{-1}\right\}R\sigma=K^aR\sigma \tag{14b}$$

where H^a and K^a are the quantities in the brackets. During plastic deformation, increments of stress/strain are used and change of the plastic mismatch ($\Delta\varepsilon^{ta}$) between each individual grain and the surrounding isotropic matrix has been expressed by **(Budiansky and Wu, 1962; Kroner, 1961)** as

$$\Delta\varepsilon^{ta}=\Delta\varepsilon^{p}-R^{-T}\Delta E^{p} \tag{15}$$

where ΔE^p is the macroscopic plastic strain increment of the bulk polycrystal with respect to the global co-ordinate system, which can be determined using the principle of virtual work **(Hu and Cocks, 2016b)**. $\Delta\varepsilon^p$ is the nominal plastic strain increment obtained from Eq. (12). Use of the matrix R^{-T} is due to the transformation between the mathematical strain and the engineering strain

(Hu, 2015). Here it is emphasized that $\Delta\varepsilon^{ta}$ would give rise to an intragranular residual stress field ΔX^a in each inhomogeneous grain, as can be obtained at the macroscopic unloading state ($\sigma = 0$ in Eq. 13)

$$\Delta X^a = C^i\left(I - S^i\right)\left(\left(C^a\right)^{-1}C^iS^i - \left(C^a\right)^{-1}C^i - S^i\right)^{-1}\Delta\varepsilon^{ta} \tag{16}$$

According to the definition in section 1, ΔX^a is a Type II meso-scale residual stress field at the grain level, not to be confused with the Type III residual stress $\left(\overline{\tau}_m^r\right)^\beta$ as described in section 2.1.3 associated with mismatch between precipitates and matrix at the slip system level. Finally, ΔX^a ($\Delta\varepsilon^p$) can be added to Eqs. (14a) and (14b) to further update the total stress σ^a and strain in each grain at each step during plastic deformation:

$$\Delta\sigma^a = H^aR\Delta\sigma + \Delta X^a \tag{17a}$$

$$\Delta\varepsilon^a = K^aR\Delta\sigma + \Delta\varepsilon^p \tag{17b}$$

The RSS is then updated using Eqs. (9) and (17a) at each time step.

3. Experimental measurement and simulation procedure

3.1 Material condition and experimental measurements

The material of interest in this study was obtained from an ex-service Type 316H F.C.C austenitic stainless steel header from a UK Advanced Gas Cooled Reactor (AGR) with the chemical composition given in Table 1. The thermal-mechanical history of this initially solution-treated material includes in-service operation of 65,015 h at an internal pressure of 40~50 MPa and temperatures of 763~803 K and an additional thermal ageing in the laboratory at 823 K for 22,100 h. The designation "EXLA" is used to describe this "Ex-service plus Laboratory Ageing" material condition. The crystallographic texture in this and similar header steels employed in this study was measured to be weak **(Chen et al., 2015b; Clausen et al., 1999)**. The material can therefore be approximated to be isotropic. Both inter- and intra-granular carbide precipitates were present in the material. The mean size (radius of equivalent spherical precipitates) and volume fraction of intragranular precipitates were estimated to be 60 nm and 0.009 based on relevant simulation and experimental work in the literature **(Chen et al., 2011; Faulkner, 2002; National Institute of**

Materials Science, 2003). The very small volume fraction of intragranular precipitates indicates that the material is essentially a single phase F.C.C. polycrystalline stainless steel. The intergranular precipitates can be ignored since they do not obstruct dislocation motion within the matrix **(Chen et al., 2011)**.

A residual stress field was introduced in the specimens by initially pre-straining each specimen at 823 K up to a stress of 250 MPa at a constant strain rate of 6×10^{-6} s^{-1}. The specimens were cooled to room temperature and unloaded. They were then subjected to either uniaxial tensile reloading (corresponding specimen designated EXLA1) or uniaxial compressive reloading (corresponding specimen designated EXLA2) at ambient temperature to assess the effect of prior deformation history on the subsequent macroscopic behaviour and associated micro-plasticity. The macroscopic deformation data employed was generated using a strain gauge and the load cell on the loading rig, while the averaged lattice response was measured using *in situ* neutron diffraction (ND). The measured change in the lattice spacing of different crystallographic planes {*hkl*} compared with the stress-free lattice spacing were transformed to give the change of elastic lattice strain. Different families of grains were measured such that the members in each family had diffracting planes with the same Miller indices {*hkl*}. The uniaxial tensile tests were conducted on the *ENGIN-X* instrument at ISIS, UK, while the uniaxial compressive tests were conducted using the *POLDI* instrument at PSI, Switzerland. A detailed description of the experimental procedure can be found in **(Chen et al., 2014; Chen et al., 2015c)**. An incremental loading history was used in the experiments with alternative loading and unloading steps adopted to measure the evolution of both the elastic lattice strain during loading and residual elastic lattice strain after unloading **(Chen et al., 2014; Clausen et al., 1999; Clausen et al., 1998; Daymond and Bouchard, 2006)**. This provides enriched data for the evaluation of residual stresses. In the present work, we focus on the axial response (diffracting planes with Miller indices parallel to the loading direction) on three major grain families - {220}, {111} and {200}.

Table 1. Chemical composition (wt.%) of Type 316H stainless steel

C	Si	Mn	P	S	Cr	Mo	Ni	Cu	N	Fe
0.07	0.61	1.65	0.025	0.007	16.6	2.33	13.6	0.26	0.025	Bal.

3.2. Simulation procedure

The response of a polycrystal to the above loading/temperature cycles was simulated using the model described in section 2. At the beginning of high temperature (HT) pre-straining, we assume

that a specimen is initially free of residual stresses and the distribution of all microstructure elements are such that the CRSS is initially identical on all slip systems in the body (identical mean spacing L_d, L_s and L_p in Eq. 2). This is reasonable since any variation of CRSS between different slip systems after service and ageing history described in section 3.1 is expected to be overwhelmed by that which can be induced by HT pre-straining. Both τ_s and τ_p were assumed to be constant throughout the simulation since the change of the population of intragranular precipitates was negligible due to the short duration of the test, which would not provide sufficient time for further nucleation, growth and coarsening of precipitates to occur. Therefore, the hardening or increase of the CRSS τ_{cr} on individual slip systems was only given by the increase of τ_d through the evolution of forest dislocation junctions (self- and latent hardening, ΔN_{self}, ΔN_{latent} in Eq. 3), taking into account the additional contribution from secondary prismatic dislocation loops punched out from the precipitates (ΔN_p in Eq. A4). The computational procedure for each loading process is shown in Fig. 4 (only shows procedure after micro-yielding). During unloading, the CRSS and all residual stresses remain the same. Further, regarding the temperature change during high temperature (HT) pre-straining and subsequent room temperature (RT) reloading, it should be noted that the shear modulus is temperature-dependent **(Frost and Ashby, 1982; Lagneborg and Forsen, 1973)**. According to **(Frost and Ashby, 1982)**

$$G = G_0\left(1+\frac{T-300}{T_M}\cdot\frac{T_M}{G_0}\frac{dG}{dT}\right) = G_0\left(1+\frac{T-300}{T_M}\cdot Y\right) \tag{18}$$

where T is the current temperature (823 K), G_0 is the shear modulus at 300 K, T_M is the melting temperature and Y is a temperature-dependence factor. For AISI 316 stainless steels, T_M=1810 K and Y= -0.81 thus G=0.766G_0 **(Frost and Ashby, 1982)**. All elastic moduli follow similar temperature dependence. Since all contributions to the CRSS are proportional to the shear modulus (Eq. 2), the CRSS needs to be scaled with the temperature-dependent modulus when the temperature changes. Similarly, all the different types of residual stress need to be scaled in a similar way with temperature. Note that additional dislocation mechanisms could occur at elevated temperatures, such as dislocation climb-controlled recovery. However, in the current problem with only short-term HT pre-straining to a small strain level, these mechanisms are expected to have minor influence on the material internal state and are not taken into account. We assess the effect of dislocation climb and recovery on the constitutive response and development of internal residual stress state for extended periods at temperature elsewhere **(Hu and Cocks, 2016a)**.

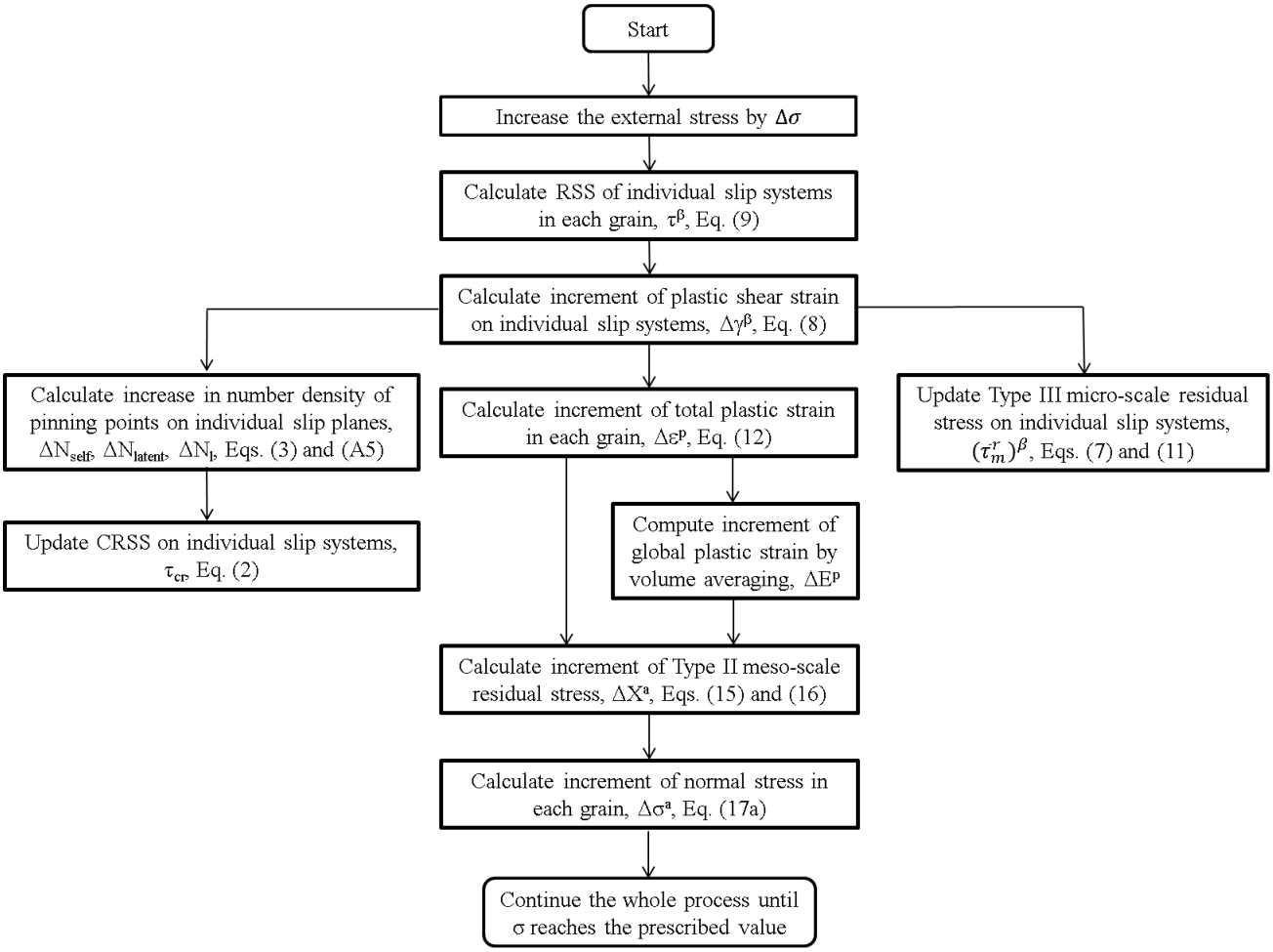

Fig. 4. Computational procedure of the self-consistent model during plastic deformation

3.3. Material parameter identification

The values of the material parameters used in the simulation are listed in Table 2, many of which have been reported and used in our previous work **(Hu and Cocks, 2016b)**. Most parameters were determined from geometric or physical requirements. The three elastic constants C_{11}, C_{12} and C_{44} of a single F.C.C. crystal are measured with respect to the local co-ordinate system, and provide the individual elements of the stiffness matrix C^a in Eq. (13) and can be used to calculate the stiffness matrix C^i (Young's modulus E, Poisson's ratio υ and bulk shear modulus G in Table 2) for the bulk polycrystal by the self-consistent procedure **(Hu and Cocks, 2016b)**. Poisson's ratio further determines the shape tensor S^i in Eq. (13) for spherical grains **(Mura, 1982)**. The obstacle strength constants are as follow: $\alpha_d = 0.35$ for forest dislocation junctions, as reported by many studies such as **(Madec et al., 2002)**; $\alpha_p = 0.84$ for a random distribution of spherical precipitates **(Foreman and Makin, 1966; Kocks, 1966)**; $\alpha_s = 0.00457$ for solute atoms **(Hu and Cocks, 2016b)**. Further, the

mean inter-precipitate spacing L_p was calculated from the estimated volume fraction (0.009) and mean radius (60 nm) of precipitates using Eq. (5). A value of 28 MPa was then obtained for τ_p at room temperature. The mean spacing between solute atoms L_s was calculated from the chemical composition of the material (all mass percent data transformed to number densities) in Table 1 using Eq. (4), assuming all elements act as weak obstacles. Depletion of solute atoms by the limited precipitation in the material has been found to be negligible. A value of 37 MPa was then obtained for τ_s at room temperature. The mean spacing L_d for forest dislocation junctions evolves during plastic deformation. Three parameters (the initial number of forest dislocation junctions on each slip plane N_0, the self-hardening coefficient j_s and the latent hardening coefficient j_l) were selected to fit the macroscopic pre-straining stress-strain curve at 823 K. All subsequent responses for room temperature reloading (in tension and compression) were then predicted by the model.

Table 2. **Material parameters of 316H austenitic stainless steel single crystals used in the simulation (RT refers to room temperature)**

Parameter	Value	Ref.	Parameter	Value	Ref.
C_{11}	198 GPa (RT)	Kamaya, (2009)	α_d	0.35	Madec et al., (2002)
C_{12}	125 GPa (RT)	Kamaya, (2009)	α_p	0.84	Ashby, (1969); Foreman and Makin, (1966); Kocks, (1966)
C_{44}	122 GPa (RT)	Kamaya, (2009)	α_s	0.00457	Hu and Cocks, (2016)
E	101.3 GPa (RT)		j_s	4.0×10^{14} m^{-2}	Hu and Cocks, (2016)
v	0.39		j_l	2.0×10^{15} m^{-2}	Hu and Cocks, (2016)
G	122 GPa (RT)		N_0	2.2×10^{13} m^{-2}	Hu and Cocks, (2016)
b	2.5×10^{-10} m		τ_s	37 MPa (RT)	Hu and Cocks, (2016)
$\Delta\gamma_0$	1	Hu and Cocks, (2016)	τ_p	28 MPa (RT)	
p	600	Hu and Cocks, (2016)			

4. Effects of Type II meso-scale intragranular residual stress on lattice deformation and the Bauschinger effect in the pre-strained specimens

4.1. Macroscopic response of the bulk polycrystal

Fig. 5 compares the measured and predicted results of the macroscopic response of the specimens

subjected to room temperature (RT) uniaxial reloading in tension (EXLA1) and compression (EXLA2), following tensile pre-straining at 823 K (data extracted from **(Chen et al., 2015c)**). For comparison, the compression data is shown using absolute values. The sharp increase of the initial yield stress observed in the RT tensile stress-strain curve (red line in Fig. 5), compared with the HT pre-straining stress-strain curve (black line in Fig. 5), is due to rescaling of the CRSS through the temperature-dependent shear modulus. These results and the predicted lattice responses (to be shown in section 4.2) are similar when we ignore the contribution of the precipitates to the constitutive response **(Chen et al., 2015c)**, indicating the weak contribution from the precipitates due to the small volume fraction in these samples. The difference between the tensile (red line) and compressive (blue line) stress-strain curves is due to different roles of the developed Type II meso-scale residual stresses from high temperature tensile pre-straining in these two specimens. In the next section, we interpret the role of Type II residual stresses in conjunction with both the development of lattice and residual lattice strains in different grain families.

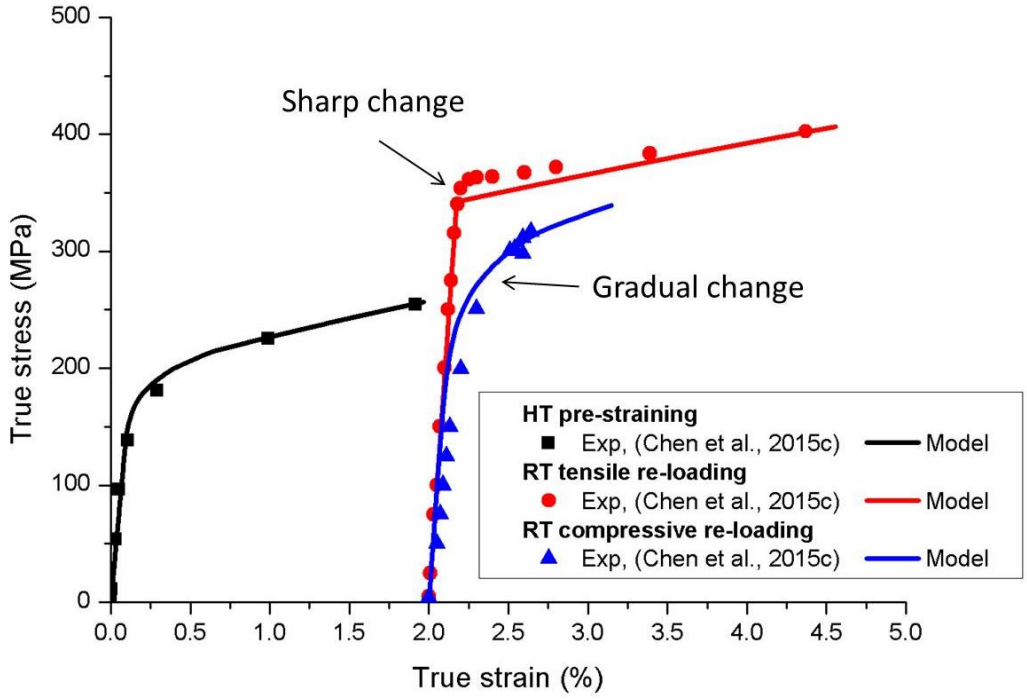

Fig. 5. Comparison of experimental data and model prediction in terms of macroscopic stress-strain relationship for EXLA specimens; the figure shows the high temperature (HT, 823 K) tensile pre-straining and the subsequent reloading in tension (EXLA1) and compression (EXLA2) at room temperature (RT). Data were extracted from **(Chen et al., 2015c)** and the prediction for EXLA2 is shown in terms of absolute stress and strain.

4.2. Microscopic lattice response of individual grain families

Fig. 6 compares the measured and predicted results of the evolution of the lattice strain during loading and the corresponding residual lattice strain upon unloading for the three grain families of interest {220}, {111} and {200} for the EXLA1 (subjected to RT uniaxial tension) and EXLA2 (subjected to RT uniaxial compression) specimens. The residual lattice strain is plotted against the macroscopic plastic strain. In these plots the reference state is that created following HT deformation and cooling to RT, thus each of the plots give the change of lattice strains with respect to this reference state. Data and predicted results for the EXLA2 specimen are again shown using absolute values to compare with those for the EXLA1 specimen. Both the data and predictions are for the response averaged over all members (with the same Miller indices) of each given family. The general experimental trends for all three grain families are predicted by the model. The model predicts an identical lattice response for all members of each family, and discontinuous changes in the slopes of the lattice response illustrated in Fig. 6 (a)-(c) indicate the occurrence of micro-yielding.

4.2.1 The role of Type II residual stress

For the tensile loaded specimen EXLA1, in Fig. 6 (a)-(c), both the measurement and prediction show an almost linear lattice strain response and small values of the residual elastic lattice strain, Fig. 6 (d)-(f) (red lines), for all three families after macroscopic yield. This indicates that a steady state Type II residual stress field has been achieved ($\Delta X^a \approx 0$ in Eqs. 16 and 17a) after the high temperature (HT) pre-straining that results in all the grains yielding simultaneously followed by compatible plastic deformation of the grains during RT reloading. A consequence of this is that there is a sharp change in slope of the macroscopic stress-strain curve at yield, as shown in Fig. 5 (red line).

In contrast, for the compressive loaded specimen EXLA2, the Type II residual stress state established during HT tensile pre-straining is significantly different from that required for all grains to deform plastically in a compatible way (the distribution and magnitude of the residual stresses are appropriate, but they have the opposite sign). Plastic flow therefore occurs much earlier in some grains than in others. The Type II residual stresses redistribute as the number of yielded grains gradually increases, leading to a gradual change in slope of the macroscopic stress-strain curve after initial yield, as shown in Fig. 5 (blue line). The lattice response for all three grain families exhibits similar features regarding the transitions in slope compared to the initial elastic portion of the curve. The first transition (the small increase in slope) suggests the onset of micro-yielding in grains

favourably orientated for slip prior to yielding in the specific grain families considered in the figure. This occurs at a macroscopic stress of 200 MPa. As these early yielding grains deform plastically, load is transferred to those that have not yet yielded (e.g. the {220}, {111} and {200} grain families). This incompatible strain mismatch gives rise to a tensile Type II residual stress and residual lattice strain in all three grain families (Eq. 16), Fig. 6 (d)-(f). This residual stress within a given grain family gradually increases until slip occurs in members of this family, resulting in a sharp decrease in the residual lattice strain as stress is transferred to other grains within the body which are yet to yield. This first occurs in the {220} grain family, then the {111} and finally the {200}. For the first two of these families, the residual lattice strain rapidly reduces to a negative value, while that for the {200} family drops less steeply and remains positive.

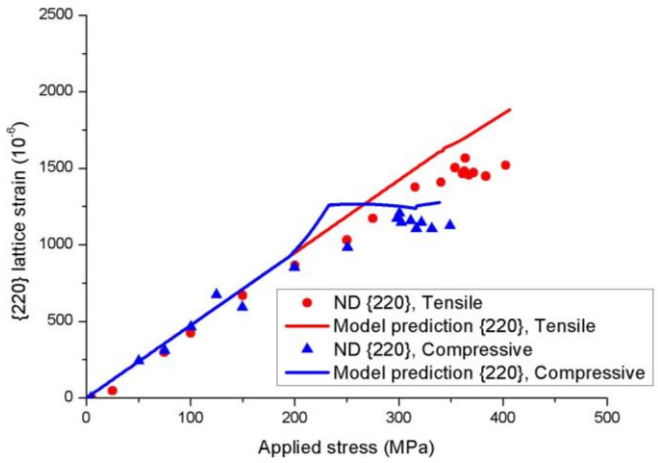

(a)

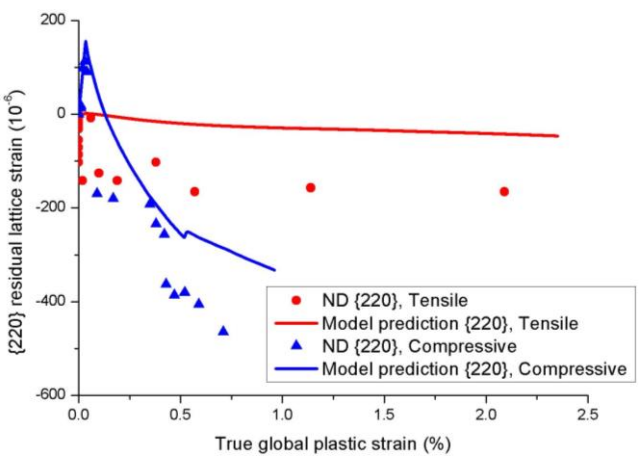

(d)

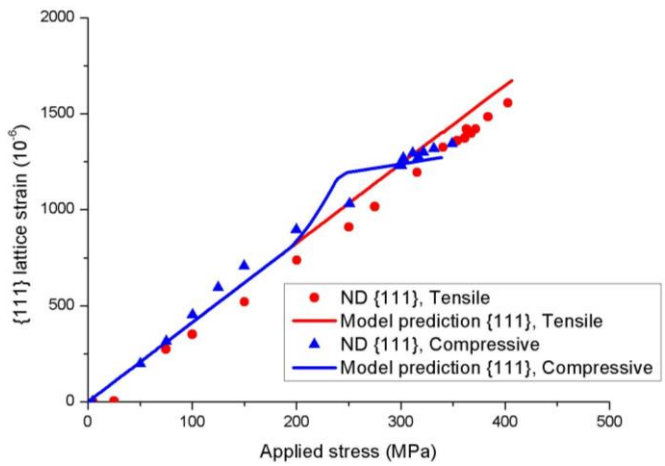

(b)

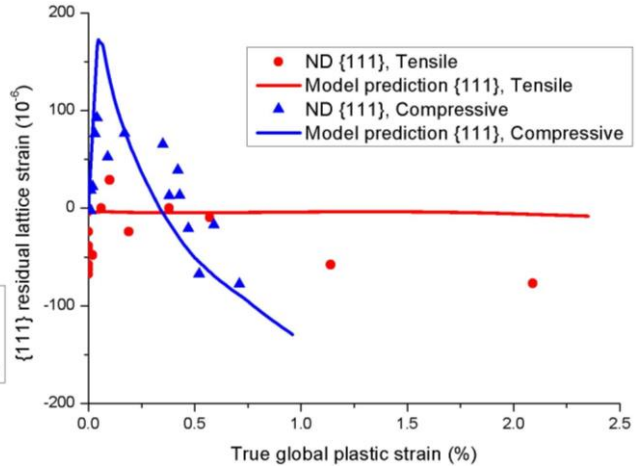

(e)

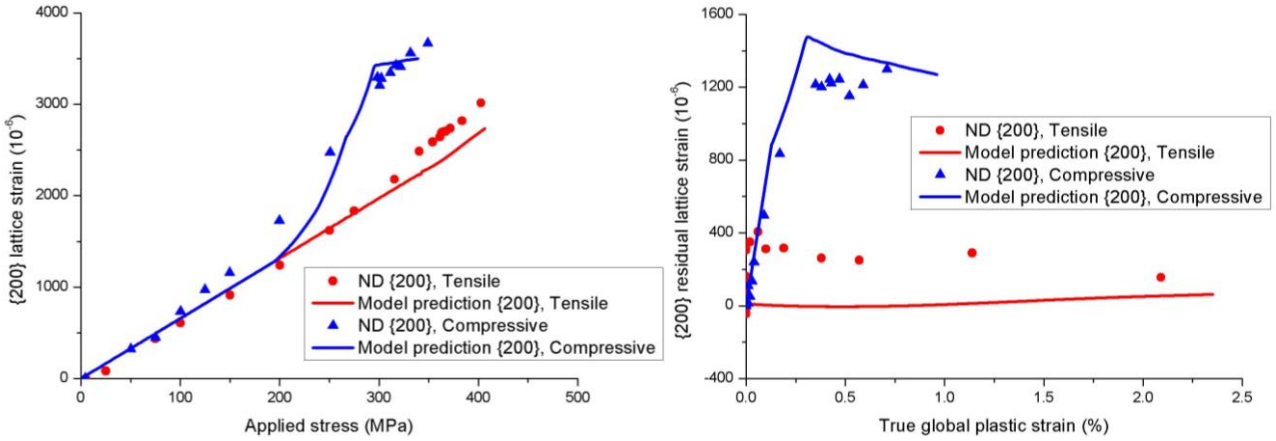

(c) (f)

Fig. 6. Measured and predicted averaged results of (a)-(c) lattice strain and (d)-(f) residual lattice strain of tensile/compressive loaded EXLA1/EXLA2 specimens (ND refers to neutron diffraction): (a) and (d) are for {220} grain family; (b) and (e) are for {111} grain family; (c) and (f) are for {200} grain family. Data and predictions for EXLA2 specimen (blue) are shown in the absolute value. The residual lattice strain is plotted against the macroscopic true plastic strain measured by the strain gauge at each unloading step.

4.2.2 The discrepancy between measurements and prediction

While the general trends observed in the experiment are captured by the model, there are discrepancies between the model predictions and the measurements. Firstly, for EXLA1, experimentally there is evidently a more distinct increase in the slope for the {200} family in Fig. 6 (c) and a sharper decrease in slope for the {220} family in Fig. 6 (a) compared with the model predictions. These differences are also reflected in the residual lattice strain response in Fig. 6 (f) and (d). This may be attributed to a number of related physical processes, such as the relaxation of the Type II residual stress field and/or creep during HT tensile pre-straining, as described by **(Chen et al., 2015c; Wilson, 1965)**. Thus, the Type II meso-scale residual stress field generated by the pre-straining may differ from the model prediction. The residual stresses therefore redistribute during the initial stages of plastic deformation towards what are required to ensure compatibility of plastic deformation, resulting in a more gradual macroscopic yielding process, Fig. 5, than the model prediction (i.e. there is a less sharp definition of yield).

Secondly, for EXLA2, it is observed that the data for all the grain families shown in Fig. 6 provides smoother transitions in slope following initiation of yield in that family compared with the predicted results. **(Hu and Cocks, 2016b)** have identified four potential aspects that may explain this, which have not been incorporated in the present model:

- The neutron diffraction technique measures specimens with a small spread of orientations when determining the lattice response of each grain family.

- The self-consistent model gives the average responses in a grain family. In practice there will be some variation due to each grain in the family having differently oriented neighbours which deform plastically at different stages of the process. However, such an effect is expected to be minor since the extent of the difference is reduced experimentally by averaging over each grain family of a full range of members with a small spread of orientation;
- The latent hardening coefficient is not constant, but evolves with plastic strain as reflected in the interaction coefficient matrix determined from discrete dislocation simulations;
- There might be a residual stress state in the specimen initially introduced by pre-processing or preloading histories applied before the high temperature pre-straining. However, the pre-straining tends to remove any pre-existing residual stresses and set up a new residual stress state, so that the subsequent response will be insensitive, or weakly sensitive, to the original residual stress state.
- A fifth effect is the effect of a distribution of link lengths on a slip plane, which can further smooth the development of residual stresses associated with different slip planes, both during tensile and compressive loading. Also, as noted by **Sleeswyk et al., (1978)**, there can be an element of back flow of dislocations held up at obstacles as the stress is reversed, before they are arrested by another set of obstacles.

The simulations can be refined to take some of these effects into account, which would result in smoothing of the transitions, but the general trends represented by Figs. 5 and 6 would remain unaltered. The form of the compressive curve in Fig. 5, particularly the onset of plastic flow where effects such as distribution of link length and back flow of dislocations are most likely to play a role, is well described by the model however.

4.3. The Bauschinger effect

Fig. 5 shows the phenomenon of transient softening (defined in Fig. 1) which is attributed to the development of Type II meso-scale residual stress fields, as discussed above. The experiments were terminated at relatively small strains, and did not allow the extent of the transient to be determined. The simulations can be extended to larger strains, as shown in Fig. 7, where the compressive curve asymptotes towards the tensile curve within an accumulated strain of 10%, indicating the absence of permanent softening in compression compared with tensile loading.

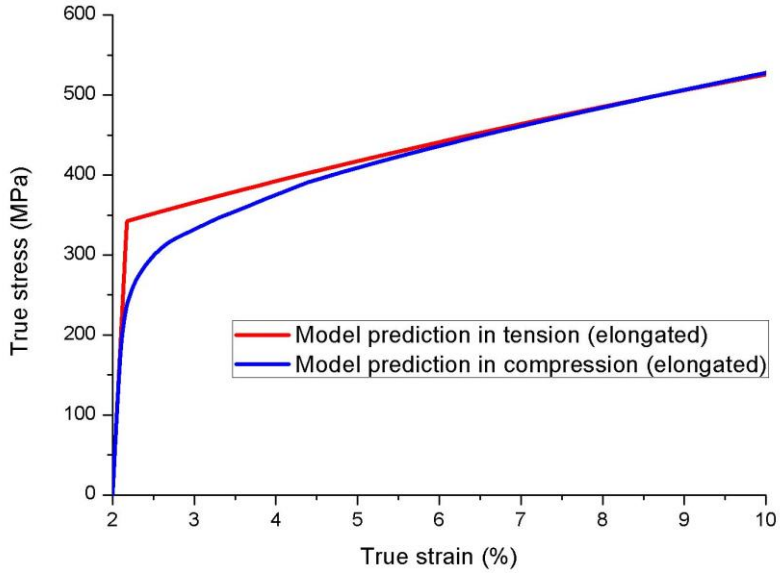

Fig. 7. Model predicted extended macroscopic stress-strain curves subjected to tensile or compressive reloading at ambient temperature. Result of the EXLA2 specimen (blue line) is shown in the absolute value.

The corresponding extended microscopic lattice responses are shown in Fig. 8. The lattice response of each of the three families of the EXLA1 specimen varies only slightly from the initial elastic lines up to large strains, while those predicted for the EXLA2 specimen eventually evolve to become parallel to the original elastic lines indicating that the Type II residual stress field has reached a steady state during which all the grains deform plastically in a compatible manner. In terms of the terminology used in the Introduction in relation to Fig 1, this result suggests that the development of Type II residual stress results in transient, and not permanent, softening.

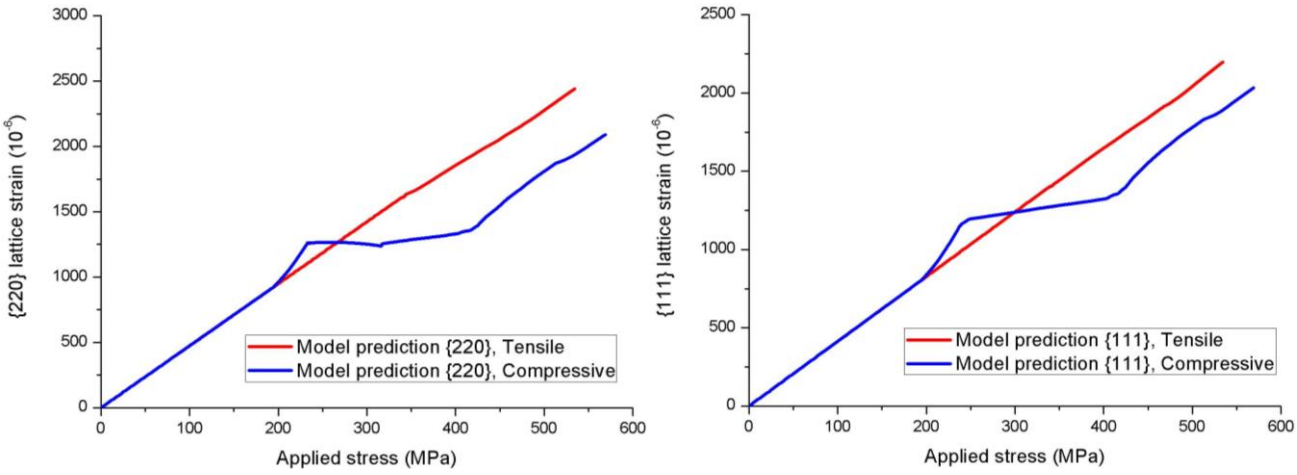

(a) (b)

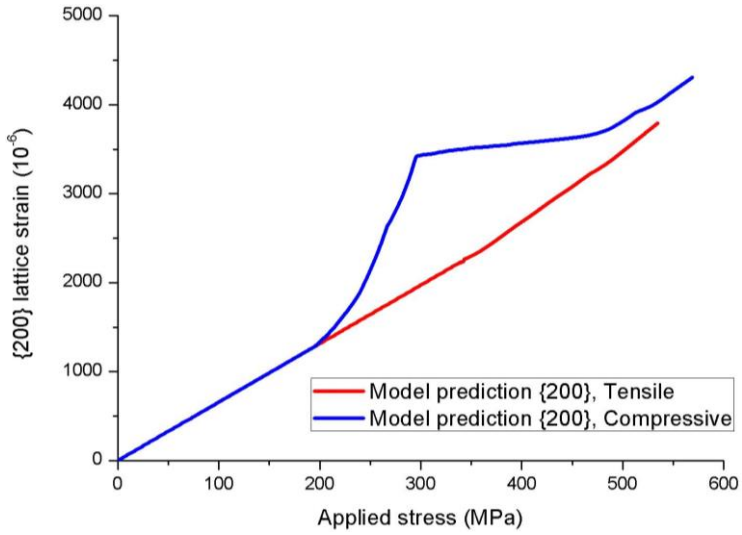

(c)

Fig. 8. Model predicted extended microscopic response subjected to uniaxial tensile or compressive reloading; (a) {220} grain family; (b) {111} grain family; (c) {200} grain family. Predictions of the EXLA2 specimen (blue lines) are shown in the absolute value.

5. Effects of Type III micro-scale residual stress on the Bauschinger effect of pre-strained specimens

This section evaluates the role of the Type III micro-scale residual stresses associated with precipitates and prismatic dislocation loops on the Bauschinger effect. According to Eqs. (7) and (11), the Type III residual stresses developed are a function of the volume fraction of intragranular precipitates and the total plastic shear strain on all the active slip systems. Therefore, the Type III residual stresses would become more significant as the volume fraction of precipitates and/or the pre-strain level is increased. Here we only focus on the macroscopic behaviour.

5.1. Effects of different volume fractions of intragranular precipitates

The Type 316H stainless steel specimens used in the experiment have been estimated to contain only 0.009 volume fraction of intragranular carbides with an average radius of 60 nm. In practice, long-term creep deformation or thermal ageing of solution-treated 316H stainless steels at elevated temperatures can result in precipitation of a range of complex phases **(Lai et al., 1981; National Institute of Materials Science, 2003; Yang and Busby, 2014)**. Depending upon the specific composition of the stainless steel and the exposure temperature and time, a combination of intragranular precipitates can be observed including intermetallic Laves and Chi phases together with $M_{23}C_6$ carbides. The equilibrium or maximum volume fraction of these two phases, together with

that of carbides, was calculated using the thermodynamics software *Thermo-Calc*, with the input of alloying elements shown in Table 1 and the phase diagram for stainless steels (detail is not shown here). Accordingly, two values of volume fraction were chosen in this section, respectively 0.05, referring to the total potential volume fraction of intragranular carbide and Laves phase, and 0.1, referring to a heavily aged material with complete precipitation of carbide and Laves plus a small amount of Chi phase. All these precipitates were treated as rigid and spherical with a size that resulted in the same spacing as in the original specimen considered above. The contributions to the internal resistance from the precipitates, including that from Orowan bowing and the punching out of prismatic loops (**Appendix B**), are therefore identical at the same strain level for all cases. Depletion of solute atoms in the austenite matrix was also calculated according to the *Thermo-Calc* results. The associated reduction of solute strengthening by the precipitation in these two cases was found to be less than 2 MPa and was neglected.

In both cases, following the original experimental procedure, the materials were initially pre-strained at 823 K up to the same strain level as the experiment (~2%). All the parameters remained the same as shown in Table 2, except the initial number of pinning points on each slip plane N_0, which was changed to provide a similar macroscopic stress-strain curve during high temperature (HT) pre-straining as the original EXLA specimen (Fig. 5). The resulting model was then used to predict the uniaxial tensile and compressive responses at room temperature and the Bauschinger effect, as shown in Fig. 9. Compared with the original results, as the volume fraction of intragranular precipitates increases, one notable observation is that the slope of both tensile and compressive stress-strain curves in the plastic region increases, indicating an increasing resistance to plastic flow by the increase of Type III micro-scale residual stress. This is because the precipitates carry an increasing proportion of the applied stress as their volume fraction is increased, thus reducing the stress carried by the matrix. The net effect is that a higher applied stress is required for dislocations to glide at a given plastic strain level. Note that the position of the sharp change in the slope of the stress-strain curve at yield during tensile reloading remains similar in all cases, since the set of assumptions employed here result in the same internal resistance or CRSS in all specimens. However, it is evident from Fig. 9 that, the Bauschinger effect, including both transient and permanent softening, becomes more and more pronounced as the volume fraction of precipitates is increased. Compared with the original result (solid blue and red curves in Fig. 9), a larger population of precipitates has resulted in a larger value of Type III micro-scale residual stress generated during HT tensile pre-straining, thus some grains start to deform plastically earlier during reverse compressive loading. A further consequence of this is that the larger Type III micro-scale residual stresses influence the evolution of the Type II residual stress field resulting in higher levels of plastic strain

being required before a steady state is achieved. However, the model always predicts a compressive curve that asymptotes to the tensile curve. The matching is delayed by an increase in population of intragranular precipitates.

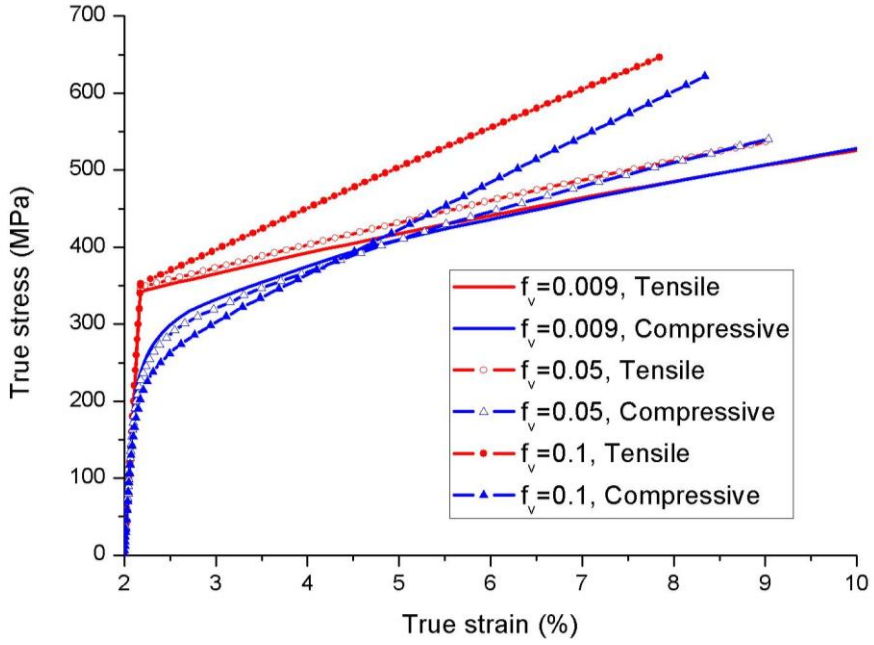

Fig. 9. Model predicted macroscopic stress-strain curves of materials with different initial volume fractions of intragranular precipitates, subjected to reloading in tension and compression at RT after HT tensile pre-straining; Predictions of the original specimen are also shown. The inter-precipitate spacing is identical for all the cases. Predictions for the compressive curves are shown in the absolute value.

5.2. Effects of different high temperature pre-strain levels

In this section, the volume fraction of intragranular precipitates is fixed at an intermediate level (e.g. 0.05) and the material is subjected to pre-strains of 2%, 4% and 6% at 823 K. The newly predicted macroscopic behaviour during subsequent tensile and compressive reloading at room temperature is shown in Fig. 10. The slope of both tensile and compressive curves in the plastic region remains almost the same, independent of the HT pre-strain level. This is because at a fixed volume fraction of precipitates, the ratio of load carried by the precipitates and that carried by the matrix remains constant. In addition, as the pre-strain level increases, the initial macroscopic yield strength increases in tension, but decreases in compression. This is due to the increase in Type III micro-scale residual stresses with increasing plastic strain, which contributes to hardening in tension, but promotes earlier plastic flow in compression. The generation of the Type III residual stress delays the onset of a steady state in the Type II residual stress, with the consequence that the strain level at which the compressive and tensile curves asymptote increases with increasing pre-strain levels.

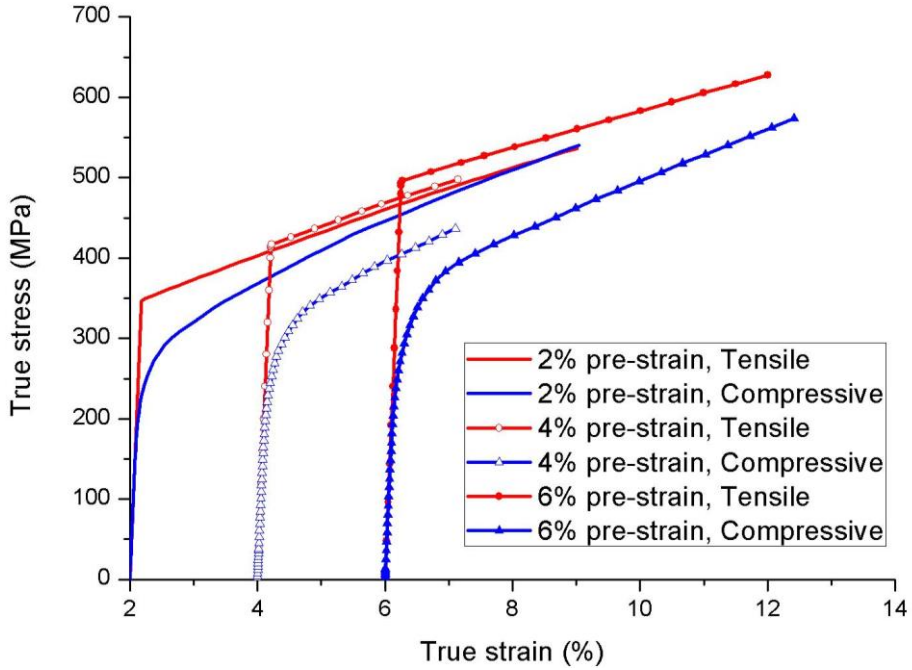

Fig. 10. Model predicted macroscopic stress-strain curves of materials with different high temperature pre-strain levels, subjected to reloading in tension and compression at room temperature after high temperature pre-straining (823 K). The volume fraction of the intragranular precipitates is fixed at 0.05. Predictions for the compressive curves are shown in the absolute value.

Further, to understand whether the enhanced softening or delayed matching between the tensile-compressive curves observed in Figs. 9 and 10 has a direct relationship to the Type II meso-scale residual stress, here we examine a material with a very large volume fraction (0.1) of intragranular precipitates. In this case, the Type III micro-scale residual stress was deactivated throughout the simulation. The material was initially pre-strained at 823 K up to a strain level of 6%, followed by the same unloading and subsequent reloading procedure as before. The result is shown in Fig. 11. No clear enhancement in the softening is observed since the two curves meet at a small strain level. Thus the Type II meso-scale residual stress field is related only to the transient softening while the Type III micro-scale residual stress field both contributes to the transient softening and delays the matching between the tensile- and compressive curves.

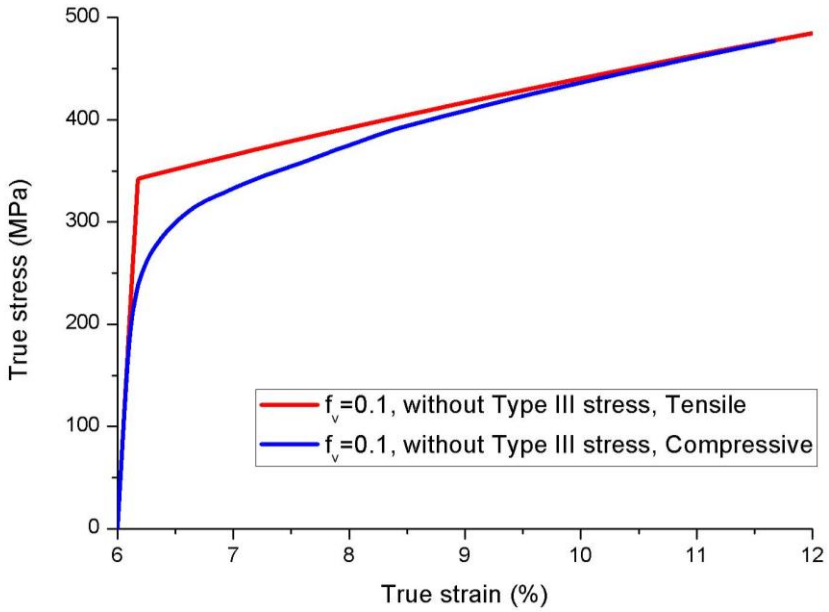

Fig. 11. Model predicted macroscopic stress-strain curves of a material with 0.1 volume fraction of intragranular precipitates and a high temperature (823 K) pre-strain level of 6%, during subsequent room temperature reloading in tension and compression. The micro-scale residual stress is ignored in the simulation. Predictions for the compressive curves are shown in the absolute value.

Lastly, it is worth noting that the findings described above for Type 316H austenitic stainless steel, i.e. asymptotic matching, has been reported by **Sleeswyk et al., (1978)** on another Type 310 stainless steel. No obvious permanent softening was observed in the material, provided a phenomenological reversible strain is deducted (interpreted as the plastic strain experienced before dislocations encounter and held up again by obstacles). Further, the distinct roles of Type II and III residual stresses on the Bauschinger effect identified in this study, seem to be similar to the findings in dual-phase ferritic steel investigated by **Kim et al., (2012)**, with the precipitates replaced by a hard phase in the dual-phase system. While these observations further validate the results of the present model in capturing the development material internal state at room temperature, they also indicate that any material with similar microstructural features to Type 316H austenitic stainless steel will exhibit a similar Bauschinger effect.

6. Concluding remarks

In this paper we have presented a self-consistent model for the plastic deformation of 316H stainless steel. The model takes into account the contributions of solute atoms, precipitates and forest dislocations on the plastic response and on the development of Type II meso-scale and Type III micro-scale residual stresses. The model has been used to evaluate the macroscopic Bauschinger

behaviour and its relationship to the development of residual stresses at the different scales. The predictions are compared with and help to explain the microscopic lattice response measured by neutron diffraction for an ex-service 316H stainless steel subjected to uniaxial tensile or compressive reloading at ambient temperature, following tensile pre-straining at 823 K. These experiments also serve to validate the model, which has been used to explore the effect of different thermal treatments (giving rise to different distributions of precipitates) and different pre-strain histories on the macroscopic Bauschinger effect. The main results and findings for polycrystalline 316H austenitic stainless steel are summarised as follows:

1. The development of Type II meso-scale residual stresses during high temperature pre-straining leads to transient softening of the material. It also explains the evolution of, and difference in, the lattice response of the three selected grain families during tensile and compressive reloading.
2. The increase in the volume fraction of intragranular precipitates and/or the pre-strain level in the material enhances the accumulation of Type III micro-scale residual stresses and delays the asymptote of the macroscopic compressive curve towards the tensile curve during reloading. This will apply to any material with microstructural features similar to 316H austenitic stainless steel.

Acknowledgements

The authors wish to express their thanks to EDF Energy Ltd for funding and supporting this research. Special thanks are given to Dr Shuyan Zhang, Instrument Scientist, ENGIN-X beamline in ISIS for experimental support and helpful discussions. The authors acknowledge the neutron diffraction beam time awards at ENGIN-X (RB1320204) and POLDI (SINQ 20111422). Peter Flewitt acknowledges Wolfson College (Oxford) for facilitating the collaboration. All authors are members of the Bristol-Oxford Nuclear Research Centre.

Appendix A. Contribution to the internal resistance by the secondary dislocation loops surrounding the precipitates

A qualitative analysis is presented here of the development of secondary prismatic dislocation loops around precipitates and how these influence further plastic flow on the different slip planes in the material. As is shown in Fig. A1, a plastic shear strain increment $|\Delta\gamma|$ (tensile and compressive has the same effect) on a given slip plane in a slab of material corresponding to the precipitate diameter $2r_p$ is achieved by the passage of *n* primary dislocations. From the geometry of this process

$$nb = 2r_p|\Delta\gamma| \tag{A1}$$

(Ashby, 1966) demonstrated that this can be accommodated by punching out n^* prismatic loops from the precipitate in each of the four secondary slip directions (Fig. 3), where,

$$n^* = \frac{n}{4} = \frac{r_p|\Delta\gamma|}{2b} \tag{A2}$$

We further assume that once generated, a loop contributes to the forest of dislocations, i.e. interactions between dislocations prevent it from flowing back to the precipitate and being recovered when the direction of shear is reversed. Therefore, the total number of additional prismatic loops per unit volume associated with slip on this slip plane is

$$4n^* \cdot N_p = \frac{2r_p|\Delta\gamma|}{b} \cdot \frac{3f_v}{4\pi r_p^{\,3}} = \frac{3f_v|\Delta\gamma|}{2\pi b r_p^{\,2}} = \frac{|\Delta\gamma|}{bL_p^{\,2}} \tag{A3}$$

where N_p and L_p are given by Eq. (5). Further, if each prismatic loop is simplified as one dislocation segment, the number of additional segments ΔN_l on this slip plane is just the two-dimensional projection of Eq. (A3)

$$\Delta N_l = \frac{|\Delta\gamma|}{bL_p^{\,2}} \cdot b = \frac{|\Delta\gamma|}{L_p^{\,2}} \tag{A4}$$

Note that ΔN_l is considered simply as the number of additional pinning points on the slip plane according to section 2.1.2. In addition, statistically a prismatic loop provides equal number of additional pinning points on all the slip planes within a grain. Therefore, Eq. (A4) is further extended as

$$\Delta N_l = \frac{\sum|\Delta\gamma|}{L_p^{\,2}} \tag{A5}$$

where the summation is over all plastic shear strain increments on all the slip planes. Finally, these additional pinning points contribute identically to the internal resistance (CRSS) on all the slip planes.

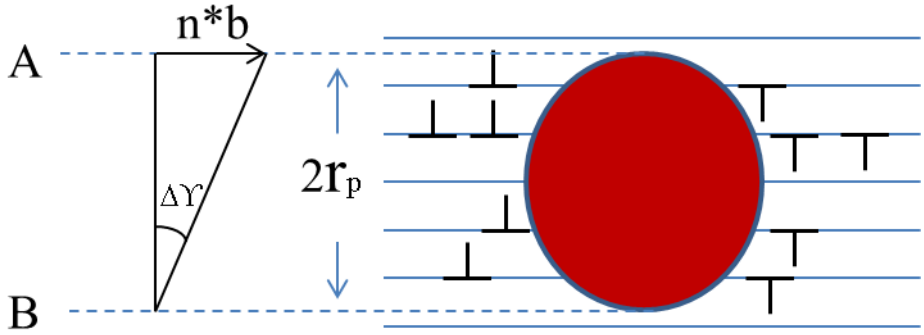

Fig. A1. A shear strain increment $\Delta\gamma$ on a pack of slip planes deposits *n* primary dislocation loops around the precipitate of radius r_p

Appendix B. Contribution to the Type III micro-scale residual stress associated with precipitates

Eq. (6) describes the stress balance on the slip plane in the unloaded state, containing an area fraction f_A (equal to the volume fraction f_v) of intersecting precipitates

$$\tau_m^r(1-f_A)+\tau_p^r f_A=0 \tag{B1}$$

We can determine the stress carried by the precipitate τ_p^r by determining the stress exerted on them by the prismatic loops. Since the stress close to a loop resembles that from a straight dislocation and falls off rapidly with distance **(Ashby, 1966; Kroupa, 1962)**, we can reasonably assume that exerted on each precipitate, τ_p^r , is dominated by that from the nearest loop. τ_p^r is analysed here based on the work of **(Kroupa, 1962)**, who took into account the average force exerted by one prismatic loop opposing the glide of a straight dislocation in its slip plane.

(Ashby, 1966) states that the secondary slip extends outward from one precipitate to a distance comparable to inter- precipitate spacing. Each new loop punched out forces the existing loops closer to each other. Consider a stack of n^* loops, as shown in Fig. B1, the outermost of which is fixed because it has reached the mid-point between precipitates or because of an earlier intersection with a gliding dislocation. The mean spacing between loops, L_l, scales with the distance between precipitates (see Eqs. 5 and A2)

$$L_l=\frac{L_p-2r_p}{2n^*}=\frac{\left(L_p-2r_p\right)b}{r_p\gamma}=\frac{b}{\gamma}\left(\sqrt{\frac{2\pi}{3f_A}}-2\right) \tag{B2}$$

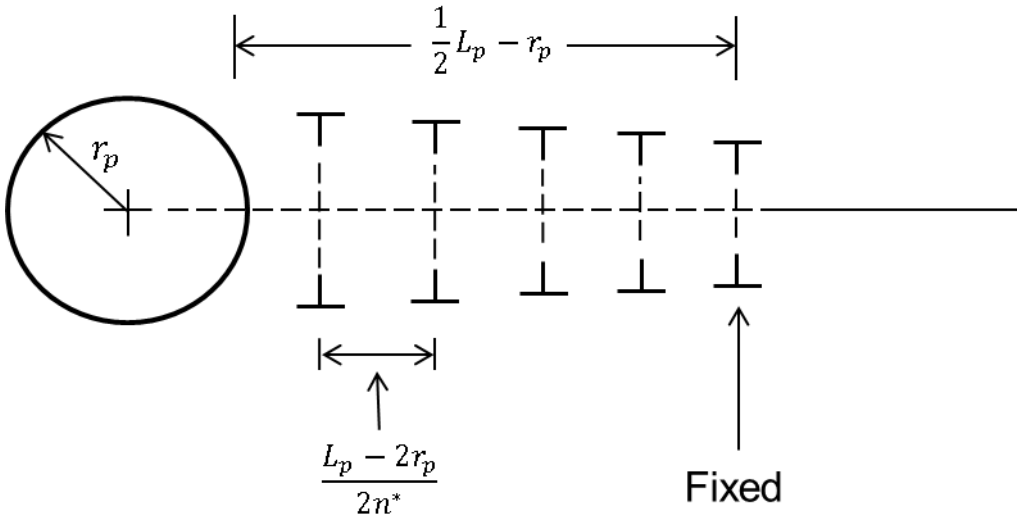

Fig. B1. A stack of prismatic loops exerts a stress in the precipitate-matrix interface which opposes the creation of another loop. This stress is roughly equal to that exerted by the nearest loop.

The stress exerted by the nearest prismatic loop is expressed by **(Kroupa, 1962)** as

$$\sigma_l = \frac{\alpha_l G b}{L_l} = \frac{\alpha_l G \gamma\left(\sqrt{3 f_A}\right)}{\sqrt{2\pi} - 2\sqrt{3 f_A}} \tag{B3}$$

where α_l is a constant (assumed here to be equal to the average strength α_d for forest dislocation junctions in Eq. 2). According to **(Ashby, 1966)** and **(Kroupa, 1962)**, each stack of loops behaves like a spring, opposing interstitial loops (tension) and attracting vacancy loops (compression). Therefore, if all the four directions with punched-out loops are considered, the stress state at precipitate-matrix interface described by Eq. (B3) is illustrated in Fig. B2 (a), which is equivalent to the pure shear stress state shown in Fig. B2 (b).

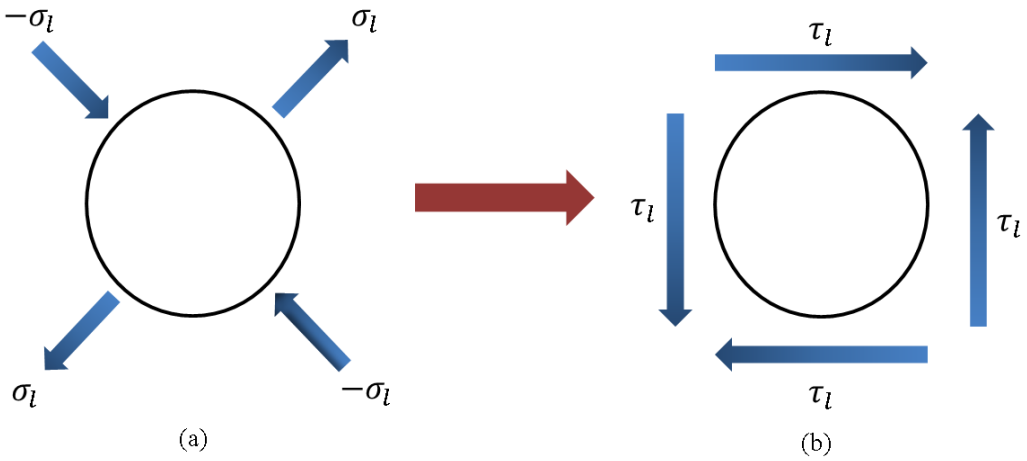

Fig. B2. The stress state of a single precipitate; (a) Attractive and repulsive stresses associated with different types of dislocation loops; (b) The equivalent pure shear stress state of the precipitate

Therefore, τ_m^r can be determined by substituting Eq. (B3) into Eq. (B2).

$$\tau_m^r = -\frac{f_A}{1-f_A}\tau_p^r = -\frac{f_A}{1-f_A}\tau_l = -\frac{\sqrt{3}\alpha_d G\gamma f_A^{3/2}}{(1-f_A)\left(\sqrt{2\pi}-2\sqrt{3f_A}\right)} \quad \text{(B4)}$$

Considering that $f_A = f_v << 1$ in stainless steel, τ_m^r can be simplified as

$$\tau_m^r \approx -0.7\alpha_d G\gamma f_A^{3/2} \quad \text{(B5)}$$

Eq. (B5) indicates that τ_m^r on a single slip plane is linearly proportional to the plastic shear strain γ on the same plane. This can be used to calculate the overall Type III residual stress on individual slip planes caused by the accumulation of plastic shear strain on all the active slip planes within the crystal plasticity framework (Eq. 11).

References

Abdel-Karim, M., Ohno, N., 2000. Kinematic hardening model suitable for ratchetting with steady-state. Int J Plasticity 16, 225-240.

Aghababaei, R., Joshi, S.P., Reddy, J.N., 2011. Nonlocal continuum crystal plasticity with internal residual stresses. J Mech Phys Solids 59, 713-731.

Alankar, A., Mastorakos, I.N., Field, D.P., Zbib, H.M., 2012. Determination of Dislocation Interaction Strengths Using Discrete Dislocation Dynamics of Curved Dislocations. J Eng Mater-T Asme 134.

Anand, L., Kothari, M., 1996. A computational procedure for rate-independent crystal plasticity. J Mech Phys Solids 44, 525-558.

Argon, A.S., 2008. Strengthening mechanisms in crystal plasticity. Oxford University Press, Oxford.

Asaro, R.J., Needleman, A., 1985. Overview .42. Texture Development and Strain-Hardening in Rate Dependent Polycrystals. Acta Metall Mater 33, 923-953.

Ashby, M.F., 1966. Work Hardening of Dispersion-Hardened Crystals. Philosophical Magazine 14, 1157-&.

Bronkhorst, C.A., Kalidindi, S.R., Anand, L., 1992. Polycrystalline Plasticity and the Evolution of Crystallographic Texture in Fcc Metals. Philos T Roy Soc A 341, 443-477.

Brown, L.M., Stobbs, W.M., 1971. Work-Hardening of Copper-Silica .2. Role of Plastic Relaxation. Philosophical Magazine 23, 1201-&.

Budiansky, B., Wu, T.T., 1962. Theoretical prediction of plastic strains of polycrystals. Proc. 4th Congr. Appl. Mech, 1175-1185.

Calhoun, R.B., Mortensen, A., 1999. Equilibrium shape of prismatic dislocation loops under uniform stress. Acta Mater 47, 2357-2365.

Chaboche, J.L., 1986. Time-Independent Constitutive Theories for Cyclic Plasticity. Int J Plasticity 2, 149-188.

Chaboche, J.L., Gaubert, A., Kanoute, P., Longuet, A., Azzouz, F., Maziere, M., 2013. Viscoplastic constitutive equations of combustion chamber materials including cyclic hardening and dynamic strain aging. Int J Plasticity 46, 1-22.

Chang, H.J., Gaubert, A., Fivel, M., Berbenni, S., Bouaziz, O., Forest, S., 2012. Analysis of particle induced dislocation structures using three-dimensional dislocation dynamics and strain gradient plasticity. Comp Mater Sci 52, 33-39.

Chen, B., Flewitt, P.E.J., Cocks, A.C.F., Smith, D.J., 2015a. A review of the changes of internal state related to high temperature creep of polycrystalline metals and alloys. Int Mater Rev 60, 1-29.

Chen, B., Flewitt, P.E.J., Smith, D.J., Jones, C.P., 2011. An improved method to identify grain boundary creep cavitation in 316H austenitic stainless steel. Ultramicroscopy 111, 309-313.

Chen, B., Hu, J.N., Flewitt, P.E.J., Smith, D.J., Cocks, A.C.F., Zhang, S.Y., 2014. Quantifying internal stress and internal resistance associated with thermal ageing and creep in a polycrystalline material. Acta Mater 67, 207-219.
Chen, B., Hu, J.N., Wang, Y.Q., Kabra, S., Cocks, A.C.F., Smith, D.J., Flewitt, P.E.J., 2015b. Internal strains between grains during creep deformation of an austenitic stainless steel. J Mater Sci 50, 5809-5816.
Chen, B., Hu, J.N., Wang, Y.Q., Zhang, S.Y., Petegem, S.V., Cocks, A.C.F., Smith, D.J., Flewitt, P.E.J., 2015c. Role of the misfit stress between grains in the Bauschinger effect for a polycrystalline material. Acta Mater 85, 229-242.
Clausen, B., Lorentzen, T., Bourke, M.A.M., Daymond, M.R., 1999. Lattice strain evolution during uniaxial tensile loading of stainless steel. Mat Sci Eng a-Struct 259, 17-24.
Clausen, B., Lorentzen, T., Leffers, T., 1998. Self-consistent modelling of the plastic deformation of FCC polycrystals and its implications for diffraction measurements of internal stresses. Acta Mater 46, 3087-3098.
Daymond, M.R., Bouchard, P.J., 2006. Elastoplastic deformation of 316 stainless steel under tensile loading at elevated temperatures. Metall Mater Trans A 37A, 1863-1873.
Deschamps, A., Brechet, Y., 1998. Influence of predeformation and ageing of an Al-Zn-Mg alloy - II. Modeling of precipitation kinetics and yield stress. Acta Mater 47, 293-305.
Devincre, B., Kubin, L., Hoc, T., 2006. Physical analyses of crystal plasticity by DD simulations. Scripta Mater 54, 741-746.
Dong, Y., Nogaret, T., Curtin, W.A., 2010. Scaling of Dislocation Strengthening by Multiple Obstacle Types. Metall Mater Trans A 41A, 1954-1960.
Eshelby, J.D., 1957. The determination of the elastic field of an ellipsoidal inclusion and related problems. Proc. R. Soc. Lond. A. 241, 376-396.
Faulkner, R.G., 2002. Microstructural examination of ex-Heysham header creep specimens. Internal report to EDF Energy.
Foreman, A.J.E., Makin, M.J., 1966. Dislocation Movement through Random Arrays of Obstacles. Philosophical Magazine 14, 911-924.
Fribourg, G., Brechet, Y., Deschamps, A., Simar, A., 2011. Microstructure-based modelling of isotropic and kinematic strain hardening in a precipitation-hardened aluminium alloy. Acta Mater 59, 3621-3635.
Friedel, J., 1964. Dislocations, Reprinted with corrections ed. Pergamon; [Distributed in USA by] Addison-Wesley Pub. Co, Oxford, Reading, Mass.
Frost, H.J., Ashby, M.F., 1982. Deformation-mechanism maps : the plasticity and creep of metals and ceramics. Pergamon Press, Oxford.
Groh, S., Zbib, H.M., 2009. Advances in Discrete Dislocations Dynamics and Multiscale Modeling. J Eng Mater-T Asme 131.
Han, C.S., Kim, J.H., Chung, K., Kang, T.J., 2006. Modeling the plastic deformation of crystals with thin precipitates. Int J Solids Struct 43, 2398-2421.
Han, C.S., Wagoner, R.H., Barlat, F., 2004. On precipitate induced hardening in crystal plasticity: theory. Int J Plasticity 20, 477-494.
Hirsch, P.B., Humphreys, F.J., 1969. Plastic deformation of two-phase alloys containing small nondeformable particles. Physics of Strength and Plasticity, 189-216.
Hirth, J.P., Lothe, J., 1982. Theory of dislocations, 2nd ed ed. Wiley, New York ; Chichester.
Hu, J., Cocks, A.C.F., 2015. Correlation between microstructure evolution and creep properties of polycrystalline austenitic stainless steel. Proceedings of 23rd Structural Mechanics in Reactor Technology (SMiRT).
Hu, J., Cocks, A.C.F., 2016a. Effect of creep on the Bauschinger effect of polycrystalline austenitic stainless steels using a thermodynamic approach. To be submitted.
Hu, J.N., 2015. A theoretical study of creep deformation mechanisms of Type 316H stainless steel at elevated temperatures. DPhil Thesis, University of Oxford.
Hu, J.N., Cocks, A.C.F., 2016b. A multi-scale self-consistent model describing the lattice deformation in austenitic stainless steels. Int. J. Solids. Struct. 78-79, 21-37.
Hu, Z.Q., Rauch, E.F., Teodosiu, C., 1992. Work-Hardening Behavior of Mild-Steel under Stress Reversal at Large Strains. Int J Plasticity 8, 839-856.
Hutchinson, J.W., 1976. Bounds and Self-Consistent Estimates for Creep of Polycrystalline Materials. Proc R Soc Lon Ser-A 348, 101-127.

Kamaya, M., 2009. A procedure for estimating Young's modulus of textured polycrystalline materials. Int J Solids Struct 46, 2642-2649.
Kim, J.H., Kim, D., Barlat, F., Lee, M.G., 2012. Crystal plasticity approach for predicting the Bauschinger effect in dual-phase steels. Mat Sci Eng a-Struct 539, 259-270.
Kocks, U.F., 1966. A statistical theory of flow stress and work-hardening. Philosophical Magazine 13, 541-566.
Kocks, U.F., 1970. Relation between Polycrystal Deformation and Single-Crystal Deformation. Metall Trans 1, 1121-&.
Kocks, U.F., 1985. Kinetics of Solution Hardening. Metall Trans A 16, 2109-2129.
Kocks, U.F., Mecking, H., 2003. Physics and phenomenology of strain hardening: the FCC case. . Progress in Materials Science 48, 171-273.
Kroner, E., 1961. On the Plastic Deformation of Polycrystals. Acta Metall Mater 9, 155-161.
Kroupa, F., 1962. Interaction between Prismatic Dislocation Loops and Straight Dislocations .1. Philosophical Magazine 7, 783-&.
Lagneborg, R., Forsen, B.H., 1973. A model based on dislocation distributions for work-hardening and the density of mobile and immobile dislocations during plastic flow. Acta Metall Mater 21, 781-790.
Lai, J.K.L., Chastell, D.J., Flewitt, P.E.J., 1981. Precipitate Phases in Type-316 Austenitic Stainless-Steel Resulting from Long-Term High-Temperature Service. Mater Sci Eng 49, 19-29.
Lee, M.G., Lim, H., Adams, B.L., Hirth, J.P., Wagoner, R.H., 2010. A dislocation density-based single crystal constitutive equation. Int J Plasticity 26, 925-938.
Li, D.F., O'Dowd, N.P., 2011. On the evolution of lattice deformation in austenitic stainless steels-The role of work hardening at finite strains. J Mech Phys Solids 59, 2421-2441.
Li, D.S., Zbib, H., Sun, X., Khaleel, M., 2014. Predicting plastic flow and irradiation hardening of iron single crystal with mechanism-based continuum dislocation dynamics. Int J Plasticity 52, 3-17.
Liu, Z.L., Zhuang, Z., Liu, X.M., Zhao, X.C., Zhang, Z.H., 2011. A dislocation dynamics based higher-order crystal plasticity model and applications on confined thin-film plasticity. Int J Plasticity 27, 201-216.
Madec, R., Devincre, B., Kubin, L.P., 2002. From dislocation junctions to forest hardening. Phys Rev Lett 89.
Miller, A.K., 1976. An inelastic constitutive model for monotonic, cyclic, and creep deformation: Part I—Equations development and analytical procedures. J Eng Mater-T Asme 96, 97-105.
Mura, T., 1982. Micromechanics of defects in solids. Martinus Nijhoff, The Hague ; London.
National Institute of Materials Science, N., 2003. Micrographs and Microstructural Characteristics of Crept Specimens of 18Cr-12Ni-Mo Stainless steel for Boiler and Heat exchanger seamless tubes (SUS 316H TB).
Neil, C.J., Wollmershauser, J.A., Clausen, B., Tome, C.N., Agnew, S.R., 2010. Modeling lattice strain evolution at finite strains and experimental verification for copper and stainless steel using in situ neutron diffraction. Int J Plasticity 26, 1772-1791.
Orowan, E., 1966. Causes and effects of internal stresses. Internal Stresses and Fatigue in Metals ed. Rassweiler and Grube, Amsterdam, Elsevier, 59.
Pham, M.S., Holdsworth, S.R., Janssens, K.G.F., Mazza, E., 2013. Cyclic deformation response of AISI 316L at room temperature: Mechanical behaviour, microstructural evolution, physically-based evolutionary constitutive modelling. Int J Plasticity 47, 143-164.
Pham, M.S., Iadicola, M., Creuziger, A., Hu, L., Rollett, A.D., 2015. Thermally-activated constitutive model including dislocation interactions, aging and recovery for strain path dependence of solid solution strengthened alloys: Application to AA5754-0. Int J Plasticity 75, 226-243.
Picu, R.C., Li, R.G., Xu, Z.J., 2009. Strain rate sensitivity of thermally activated dislocation motion across fields of obstacles of different kind. Mat Sci Eng a-Struct 502, 164-171.
Queyreau, S., Monnet, G., Devincre, B., 2009. Slip systems interactions in alpha-iron determined by dislocation dynamics simulations. Int J Plasticity 25, 361-377.
Queyreau, S., Monnet, G., Devincre, B., 2010. Orowan strengthening and forest hardening superposition examined by dislocation dynamics simulations. Acta Mater 58, 5586-5595.
Sleeswyk, A.W., James, M.R., Plantinga, D.H., Maathuis, W.S.T., 1978. Reversible Strain in Cyclic Plastic-Deformation. Acta Metall Mater 26, 1265-1271.
Taleb, L., Cailletaud, G., Sai, K., 2014. Experimental and numerical analysis about the cyclic behavior of the 304L and 316L stainless steels at 350 degrees C. Int J Plasticity 61, 32-48.
Wilson, D.V., 1965. Reversible Work Hardening in Alloys of Cubic Metals. Acta Metall Mater 13, 807-&.

Withers, P.J., Bhadeshia, H.K.D.H., 2001a. Overview - Residual stress part 1 - Measurement techniques. Mater Sci Tech Ser 17, 355-365.
Withers, P.J., Bhadeshia, H.K.D.H., 2001b. Overview - Residual stress part 2 - Nature and origins. Mater Sci Tech Ser 17, 366-375.
Yang, Y., Busby, J.T., 2014. Thermodynamic modeling and kinetics simulation of precipitate phases in AISI 316 stainless steels. J Nucl Mater 448, 282-293.
Yoshida, F., Uemori, T., Fujiwara, K., 2002. Elastic-plastic behavior of steel sheets under in-plane cyclic tension-compression at large strain. Int J Plasticity 18, 633-659.
Yu, C., Kang, G.Z., Kan, Q.H., 2014. Crystal plasticity based constitutive model for uniaxial ratchetting of polycrystalline magnesium alloy. Comp Mater Sci 84, 63-73.